

15

Properties of Oxide Surfaces

Martin Sterrer and Hans-Joachim Freund

15.1

Introduction

Oxides comprise a very diverse class of compounds with properties covering almost all aspects of material science and physics. Oxides can be both superconductors and insulators. The bonding characteristics may be classified as covalent for one system and highly ionic for the other. Oxides find applications in many fields of technical interest, from paint pigments via nonlinear optics to sensors and catalysis. In some cases, the bulk properties are important, as, for example, very often in nonlinear optics; in other cases, the surface properties play a major role, as in catalysis.

The bulk properties of simple binary oxides are pretty well understood and there are excellent reviews and books available treating the thermodynamics, the structure – and its nonstoichiometric aspects, which are particularly important for oxides – the spectroscopy, and the transport and mechanical properties [1–6]. Bulk properties of even more complicated oxides such as ternary and quaternary oxides are being intensively investigated, partly due to their importance in high- T_c superconductivity [7].

While the bulk properties of simple binary oxides are well understood, rather little is known about the surfaces of oxides, even the most simple ones. Only recently, if compared with the 30 years of surface science that have passed by [8], researchers have started to study the surface science of oxides. There is a very useful book by V. E. Henrich and P. A. Cox that marks the first milestone in this effort entitled “The Surface Science of Oxides” [9]. Since the publication of this book, several reviews have appeared that have covered the field up to the present date [10–16]. It is understood that there are classes of technologically very important oxides exhibiting external and internal surfaces, that is, zeolites and mesoporous materials, which will not be discussed here. We refer the reader to a recent article by Thomas *et al.* [17]. This chapter will treat the properties of single crystalline oxide surfaces in terms of their geometric and electronic structure.

15.2

Geometric Structure of Oxide Surfaces

15.2.1

Bulk Crystal Structures

Before considering the structure of oxide surfaces, it is useful to examine the bulk structure of oxides. Stoichiometry and coordination are the most important factors that determine the oxide crystal structure. The most common stoichiometries of binary oxides are MeO , MeO_2 , Me_2O_3 , and Me_3O_4 . Ternary oxides appear as Me(I)Me(II)O_3 and $\text{Me(I)Me(II)}_2\text{O}_4$. In almost all cases, the metal ions are surrounded by either six or four oxygen ligands, giving either octahedral (Figure 15.1a) or tetrahedral (Figure 15.1b) coordination, respectively.

One can construct oxide structures by assuming either a face-centered cubic (fcc) or hexagonal close-packed (hcp) lattice of oxygen ions and filling the vacant octahedral or tetrahedral interstitial sites with metal ions. Figure 15.1c,d shows the possible vacant octahedral and tetrahedral interstitial sites for an fcc and

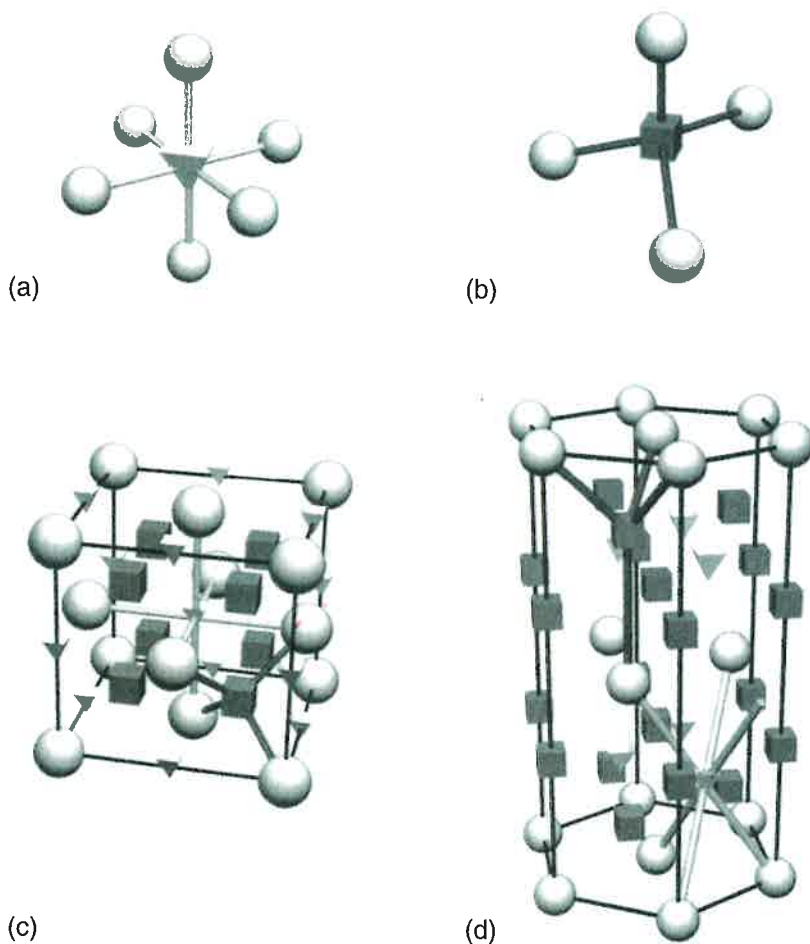


Figure 15.1 (a,b) Coordination polyhedra for metal cations octahedrally and tetrahedrally coordinated by oxygen ions. (c,d) Interstitial sites in an fcc and hcp lattice, respectively (pyramids, octahedral interstitial sites; cubes, tetrahedral interstitial sites).

Table 15.1 Most common oxide crystal structures and examples.

Name	Examples
Rock salt	MgO, NiO, MnO, CoO, FeO
Fluorite	CeO ₂ , ZrO ₂
Spinel	Al ₂ MgO ₄ , Fe ₃ O ₄ (inverse)
Perovskite	SrTiO ₃ , BaTiO ₃ , NaWO ₃
Wurtzite	ZnO, BeO
Rutile	TiO ₂ , RuO ₂ , SnO ₂
Corundum	Al ₂ O ₃ , Fe ₂ O ₃ , Cr ₂ O ₃ , V ₂ O ₃ , Ti ₂ O ₃

hcp lattice, respectively. A close inspection of Figure 15.1c,d reveals that in both cases, one octahedral site and two tetrahedral sites per oxygen ion are available. Starting from the close-packed fcc and hcp array, one can realize the structure of oxides with different stoichiometry and coordination by filling the interstitial sites appropriately. The most important classes of oxide crystal structures and typical examples are summarized in Table 15.1.

A 1:1 stoichiometry of metal and oxygen ions (MeO) is obtained by filling the octahedral interstitial sites in an fcc lattice (rock salt) or by occupying one-half of the tetrahedral interstitial sites in an hcp lattice (wurtzite). The rock salt structure represents interpenetrating fcc cation and anion sublattices where the cations are surrounded by six nearest neighbor oxygen ions (Figure 15.2a). In the hexagonal wurtzite structure (Figure 15.2e), the metal coordination is 4.

Filling all tetrahedral holes in an fcc lattice and reversing the arrangement of anions and cations gives the fluorite structure (MeO₂, Figure 15.2b) found for CeO₂ and ZrO₂. Note that here the metal coordination is 8. The same stoichiometry (MeO₂) is obtained by starting from an hcp lattice of oxygen ions and filling only half of the octahedral interstitial sites. The most prominent representatives of the so-formed rutile structure ($Z = 6$, Figure 15.2f) are TiO₂ and SnO₂.

The ideal perovskite structure is cubic and adopted by oxides with ABO₃ stoichiometry (e.g., CaTiO₃), where the A metal sits on the corners of the cube and is 12-fold coordinated by oxygen, which are located on the faces. The B cation, which is usually a transition metal ion, occupies the center of the cube (Figure 15.2c).

The corundum structure (M₂O₃, e.g., Al₂O₃, Fe₂O₃) is realized by filling two-thirds of the octahedral sites in an hcp lattice of oxygen ions. Between two oxygen rows, there is a metal layer where every third site is unoccupied. The metal atoms in this layer form hexagons with the center being empty. The stacking sequence of the metal layers is ABCABC (Figure 15.2g).

The spinel structure is a cubic structure with one-half of the octahedral and one-eighth of the tetrahedral sites in an fcc oxygen lattice being occupied. In the normal spinel, one type of metal sits on the octahedral site and another metal ion on the tetrahedral sites giving a stoichiometry of Me(I)Me(II)₂O₄, for example, MgAl₂O₄. On the other hand, in the inverse spinel structure, only one type of metal with

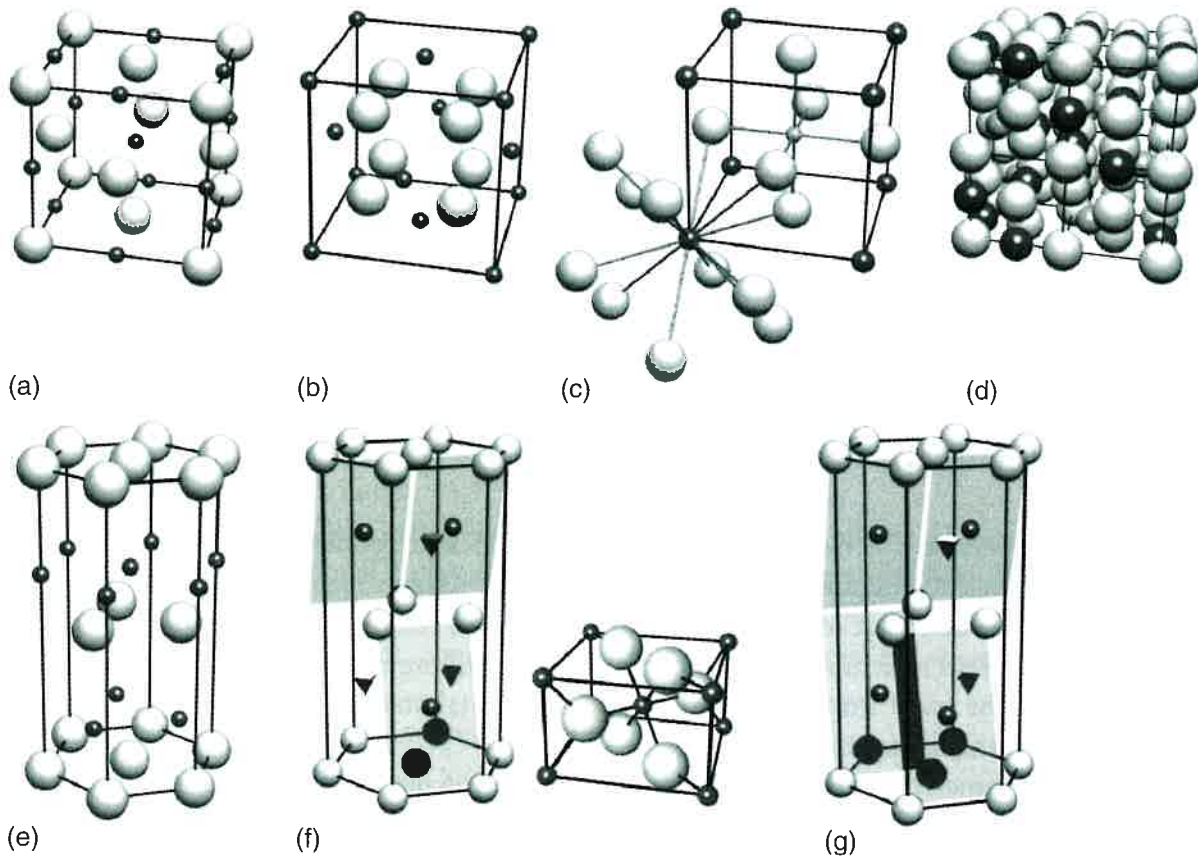


Figure 15.2 Most common bulk crystal structures of oxides (oxygen ions, light spheres; metal ions, dark spheres): (a) rock salt, (b) fluorite, (c) perovskite, (d) inverse spinel, (e) wurtzite, (f) rutile, and (g) corundum.

mixed valence is distributed over the interstitial sites. The most common example is Fe_3O_4 , where Fe^{2+} occupies the octahedral site and Fe^{3+} ions are distributed equally among the tetrahedral and remaining octahedral sites (Figure 15.2d).

15.2.2

The Geometric Structure of Oxide Surfaces

Starting from the three-dimensional bulk lattice, we can, in principle, generate oxide surfaces by cutting the crystal along any crystal plane. In this manner, an ideally bulk-truncated surface is obtained, which means that the atomic positions do not change on cleavage. In practice, however, there are only a few cleavage planes that yield stable surface structures, and surface atomic positions can differ substantially from the corresponding bulk ones.

The practically most important cleavage planes and surface orientations of oxide surfaces are depicted in Figure 15.3. These are the (100), (110), and (111) planes in case of a cubic lattice, and the (0001), (10–10), and (11–20) planes for a hexagonal lattice. The most important quantity that relates to the stability of a given surface orientation is the surface energy, which is defined as the work needed to cut a bulk crystal into two equivalent parts. In a simple way, one could think of the surface

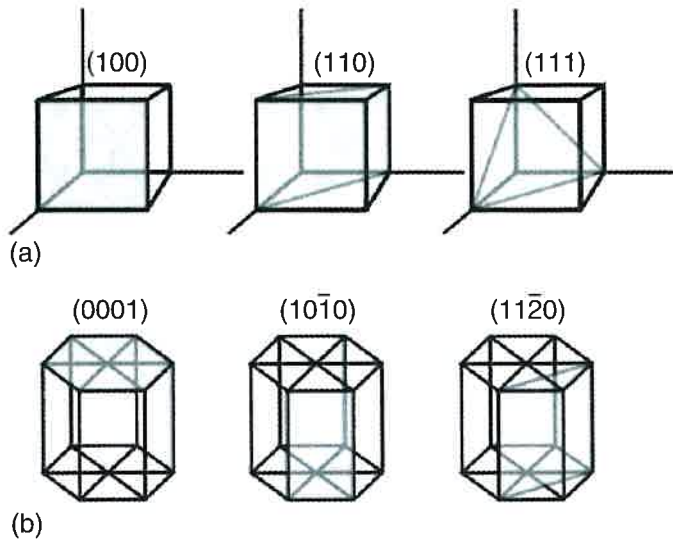


Figure 15.3 Low-Miller-index planes in a (a) cubic and (b) hexagonal lattice.

energy as the number of bonds that need to be broken per surface atom or, in an ionic picture, as the number of missing neighbors in the first coordination sphere. For example, consider a crystal with rock salt structure cut along the (100), (110), and (111) orientations. For a cut along (100), every surface ion misses only one ion with respect to the ideal bulk coordination (Figure 15.4a), whereas the number of missing neighbors increases to two and three for (110) and (111) surfaces, respectively. Hence, the (100) plane is the most stable surface orientation found for oxides with the rock salt structure.

The formation of a surface by separating a crystal with rock salt structure is straightforward, because a cut perpendicular to the (100) crystal direction results always in the formation of two equivalent rock salt (100) surfaces, exhibiting the same surface structure and number of ions. However, the situation becomes more difficult for oxide structures with a more complex stacking sequence. In Figure 15.4b, we show three possibilities to separate a crystal with rutile structure

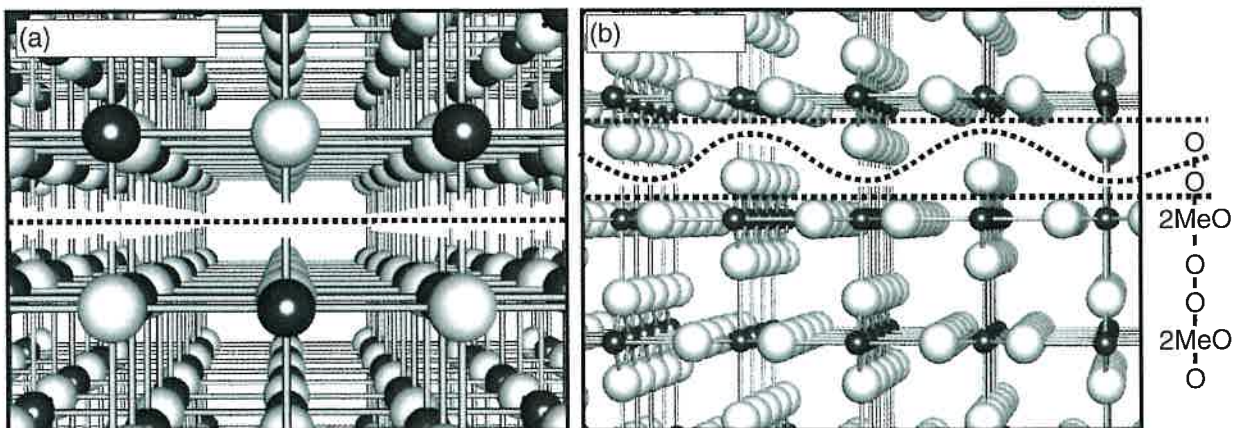


Figure 15.4 (a) Cut perpendicular to the (100) direction of a crystal with rock salt structure. (b) Different possibilities (dotted lines) for cutting a crystal with rutile structure perpendicular to the (101) direction.

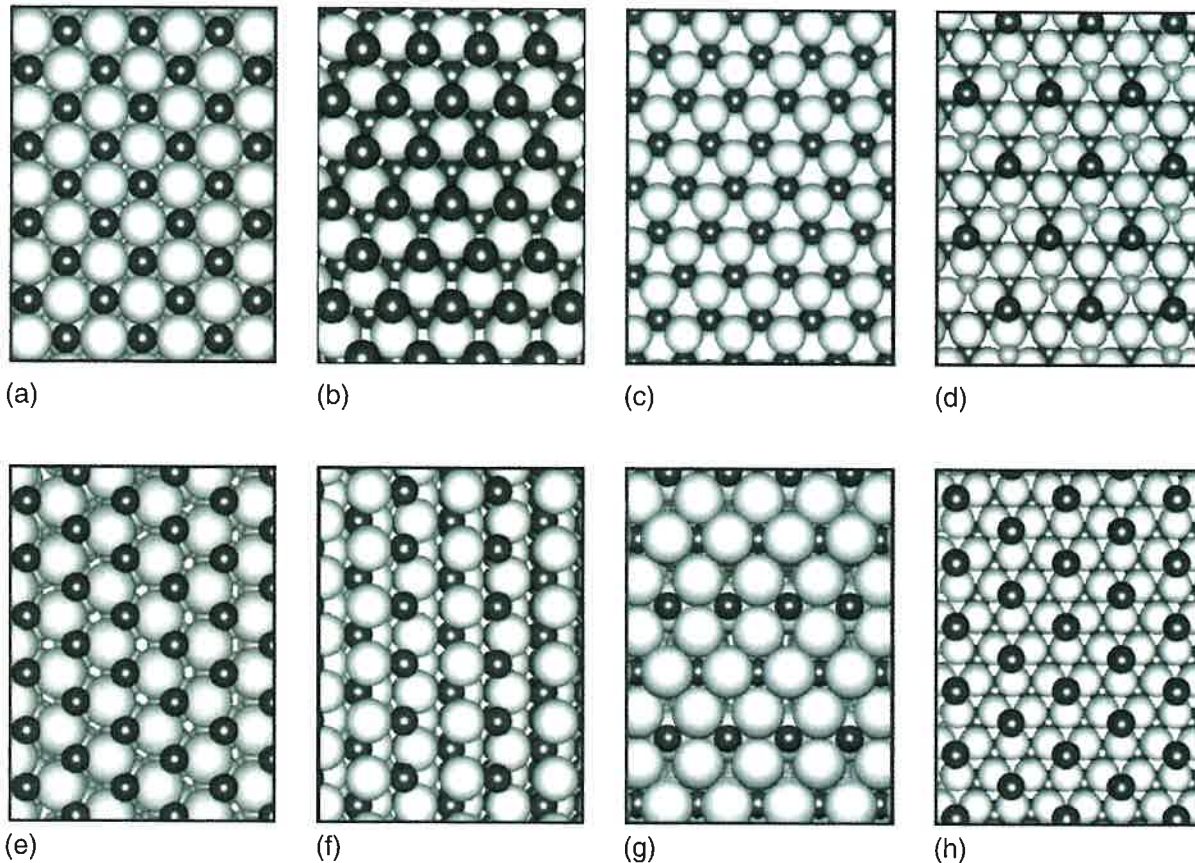


Figure 15.5 Most common surface structures of oxides (oxygen ions, light spheres; metal ions, dark spheres): (a) rock salt (100), (b) rock salt (111), (c) fluorite (111), (d) inverse spinel (111), (e) wurtzite (0001), (f) wurtzite ($10\bar{1}0$), (g) rutile (110), and (h) corundum (0001).

to create a (110) surface (dotted lines). The stacking sequence in rutile along the (110) direction is $-O-2MeO-O-O-2MeO-$. One could, therefore, imagine separating the crystal to obtain a $-O-2MeO$, $-O-2MeO-O$, or $-O-2MeO-O-O$ terminated surface. Upon those three possibilities, only a cut that yields the $-O-2MeO-O$ termination gives two equivalent and stoichiometric surfaces.

Figure 15.5 is a representation of the most common ideally bulk-truncated surface structures of oxides. Here, we consider the structure of the surface as being an ideal cut through a bulk crystal plane with the surface ions remaining in positions that they would otherwise have in the bulk. However, in reality, the atomic positions of the outermost surface layers are, due to the surface boundary, often subject to considerable displacement. We will discuss processes that lead to such displacements as well as concepts of surface stability in the proceeding paragraphs. Additionally, any surface plane is never a perfect infinitely extended plane but rather consists of terraces that are separated by monoatomic steps. On the terraces and on steps, a number of defects can exist, the most important ones are vacancies, as shown in Figure 15.6. The structural properties of defects and their influence on the electronic structure of the oxide will be discussed in the following.

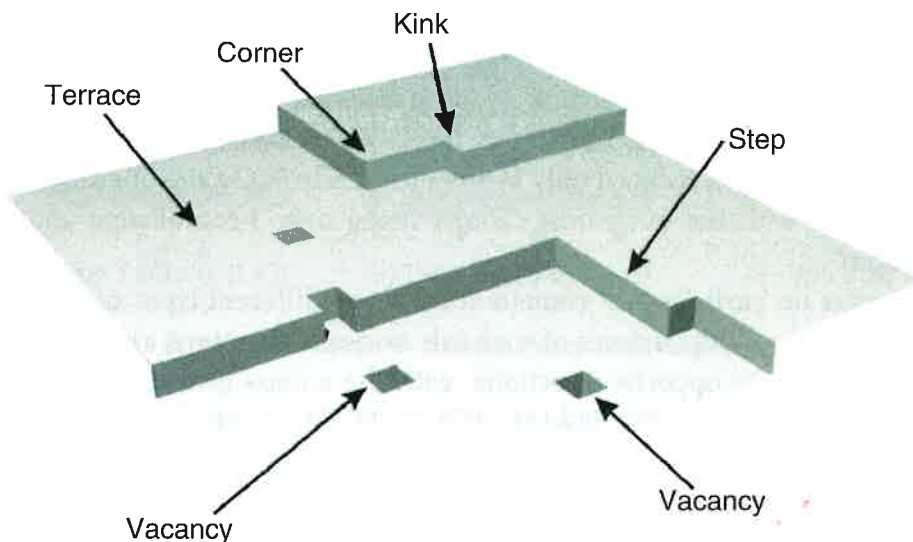


Figure 15.6 Model of a surface containing steps and point defects.

15.2.2.1 Relaxation, Rumpling, and Reconstruction

Until now, we viewed the surface of oxides as a truncation of the bulk three-dimensional lattice; that is, we assumed that the surface ions are on positions that they would also have in the oxide bulk. However, the creation of the surface includes the breaking of bonds, and consequently, additional forces acting on the outermost layers can push the surface ions out of their ideal bulk positions leading to structural distortions known as *relaxation*, *rumpling*, and *reconstruction* (Figure 15.7; see Ref. [10] for a general discussion). In general, these phenomena lead to a lowering of the surface energy of a given surface and, therefore, to increased stability of the surface.

A *relaxation* corresponds to a change in the interlayer spacing of the outermost surface layers as compared to the bulk layers (Figure 15.7a). For most surface structures of oxides, an inward relaxation of the surface layer is observed, corresponding to a contraction of the interlayer spacing. Surface relaxation may affect several surface layers and decays exponentially into the bulk. In the simplest case of the ionic limit, surface relaxation can be explained by the reduced coordination number and, consequently, the reduced Madelung energy of surface ions. With

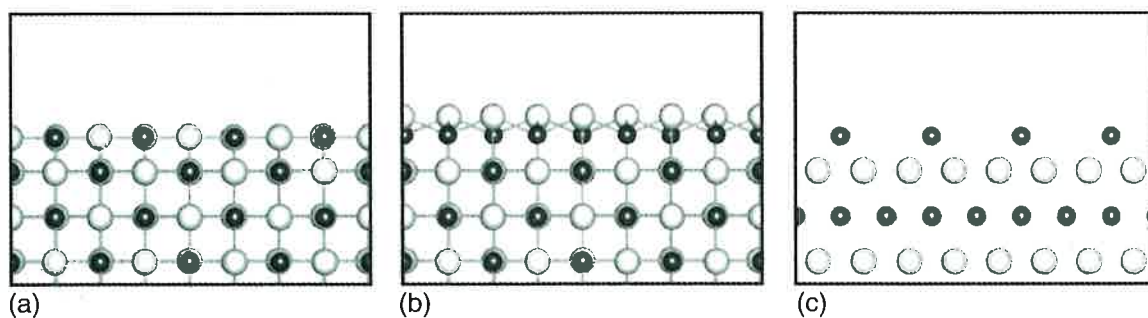


Figure 15.7 Schematic representation of (a) relaxation, (b) rumpling, and (c) reconstruction.

decreasing coordination number, the interatomic distance decreases, provided the electrostatic attraction (the Madelung energy) dominates the short-range repulsion, thereby leading to bond contraction. As a consequence, relaxation effects are smallest for densely packed surfaces such as the (100) rock salt surfaces, where the coordination number is reduced only by one, from 6 to 5. On the other hand, corundum surfaces with the outermost cations being only 3-coordinated show strong relaxation.

Rumpling occurs on surfaces that contain at least two different types of atoms as, for example, on the (100) surfaces of rock salt oxides. The anions and cations are vertically displaced in opposite directions, with the anions generally moving outward and the cations moving inward (Figure 15.7b). In the ionic model, this effect can be explained by different electrostatic forces acting on cations and anions, resulting from different polarizabilities that add to the Madelung energy.

A different mechanism that includes bond rotation rather than bond length changes has been proposed for more covalently bonded oxides [18].

As discussed earlier, both surface relaxation and rumpling are associated with changes in interatomic distances, thereby retaining the bulk periodicity of atoms on the surface. A different situation occurs when the oxide surface undergoes a *reconstruction* (Figure 15.7c). Here, the surface layer possesses a different periodicity than the bulk and even the stoichiometry may be changed. The driving force for surface reconstruction is again a lowering of the surface energy, which can have different kinds of origin. On one hand, electronic effects such as the inherent instability of polar surfaces (see later discussion) due to the infinite dipolar moment may give rise to surface reconstruction, for example, on rock salt (111) surfaces. On the other hand, thermodynamic arguments such as annealing temperature or oxygen partial pressure are responsible for the observation of different atomic structures of oxide surfaces.

We note that reconstruction is not limited to the first surface layer. In particular, in ionic crystals and semiconductors, it may reach up to 10 layers into the bulk. This is different from metals where screening limits reconstruction to the first few layers.

15.2.2.2 Stability of Oxide Surfaces

Considering an ionic model with metal and oxygen having positive and negative charges, respectively, Tasker [19] proposed a classification of oxide surfaces based purely on electrostatic criteria. In this model, the crystal is represented by a stack of planes perpendicular to the surface. The planes are arranged in a way to give an electrostatically neutral building block, which builds up the whole crystal. The surfaces are classified by the net charge Q in a plane and the dipole moment μ of the building block perpendicular to the surface.

The surface of, for example, the rock salt (100) or (110) plane contains equal numbers of cations and anions and possesses, therefore, no net charge ($Q = 0$). The repeat unit indicated by the square bracket in Figure 15.8a exhibits no dipole moment perpendicular to the surface ($\mu = 0$), yielding a nonpolar type 1 surface.

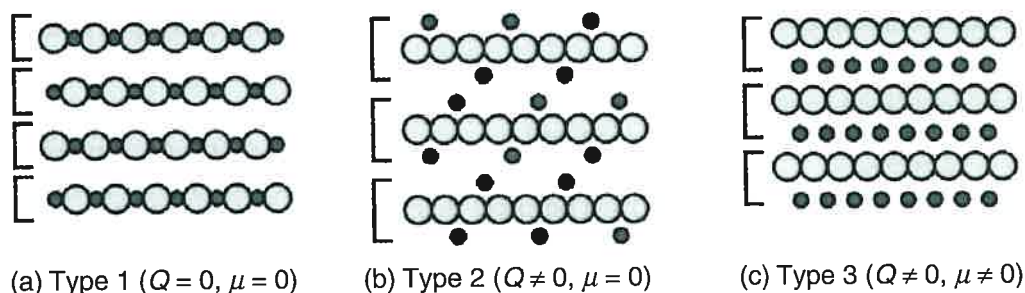


Figure 15.8 (a–c) Classification of oxide surfaces according to Tasker [19].

On type 2 and type 3 surfaces, on the other hand, the individual planes contain only one particular type of ion and are, therefore, not charge neutral ($Q \neq 0$). On a type 2 surface, however, the bulk repeat unit may be constructed such that the net dipole moment perpendicular to the surface vanishes ($\mu = 0$), resulting in a nonpolar surface. This is shown in Figure 15.8b. Typical examples of type 2 surfaces are the (0001) plane of corundum and the (110) surface of rutile. In the case of type 3 surfaces, the building block always possesses a net dipole moment perpendicular to the surface ($\mu \neq 0$), for example, the (111) surfaces of the rock salt structure. These are polar surfaces (Figure 15.8c).

Polar type 3 surfaces are unstable due to the diverging electrostatic energy caused by the finite dipole moment in all building blocks. However, there are several examples of naturally occurring minerals that expose polar surfaces, for example, MgO(111) and NiO(111) or ZnO(0001). The mechanisms that lead to stabilization of polar surfaces necessarily involve charge modifications of the surface layers. There are several ways to achieve the charge modifications of polar surfaces [20]:

- 1) Strong surface relaxation may reduce or compensate the excess surface charge.
- 2) The stoichiometry of the surface may change in order to provide charge compensation. This can be achieved, for example, by the formation of an ordered array of vacancies and is generally known as *surface reconstruction*.
- 3) The charge state of the surface may be changed by adsorption of atoms or ions on the surface. As polar oxide surfaces are highly reactive, adsorption of gases from the residual background, even under ultrahigh-vacuum (UHV) conditions, can take place on a very short time scale.
- 4) The transfer of electrons from the negative to the positive surface.

15.2.2.3 Chemical Potential of Oxygen

The actual surface termination of oxides not only is a result of relaxation or reconstruction but also depends critically on the environment. Preparation of oxide surfaces for UHV studies often requires high-temperature or high-pressure oxygen treatment. Such factors can lead to dynamic adsorption/desorption processes, which determine the surface structure under these conditions. At given experimental parameters, the surface structure with the lowest surface free energy will be the most stable one. A formalism has been developed that allows the calculation of the surface free energy from *ab initio* methods as a function of pressure and

temperature using the Gibbs free energy G as thermodynamic quantity [21]. The surface free energy γ at given p and T can be defined as

$$\gamma = \frac{1}{A} \left[G(T, p, N_i) - \sum N_i \mu_i(T, p) \right] \quad (15.1)$$

where A is the surface area, μ_i is the chemical potential of metal and oxygen ions, and N_i is the number of metal and oxygen ions. This equation can be reformulated so that instead of the Gibbs free energy, the calculated total energies of the system enter and the pressure dependence is only given by the chemical potential of the gaseous component, that is, oxygen, the temperature and pressure dependence of which is calculated using the well-known thermodynamic relation

$$\mu_{\text{O}}(T, p) = \mu_{\text{O}}(T, p^0) + \frac{1}{2kT} \ln \left(\frac{p}{p^0} \right) \quad (15.2)$$

As an example, Figure 15.9 shows the results obtained for different oxygen chemical potentials for different surface structures of the rutile (110) surface, here the specific case of $\text{RuO}_2(110)$, which is a metallic oxide [21]. As discussed earlier (Figure 15.4), there are three possibilities for rutile (110) termination. The most stable configuration is the one with bridging oxygen, $\text{RuO}_2(110)\text{-O}^{\text{bridge}}$, because this is an uncharged surface with the least number of broken bonds. By adding to this surface oxygen ions that occupy atop sites of the undercoordinated Ru ions, the surface becomes oxygen terminated with two types of low-coordinated oxygen,

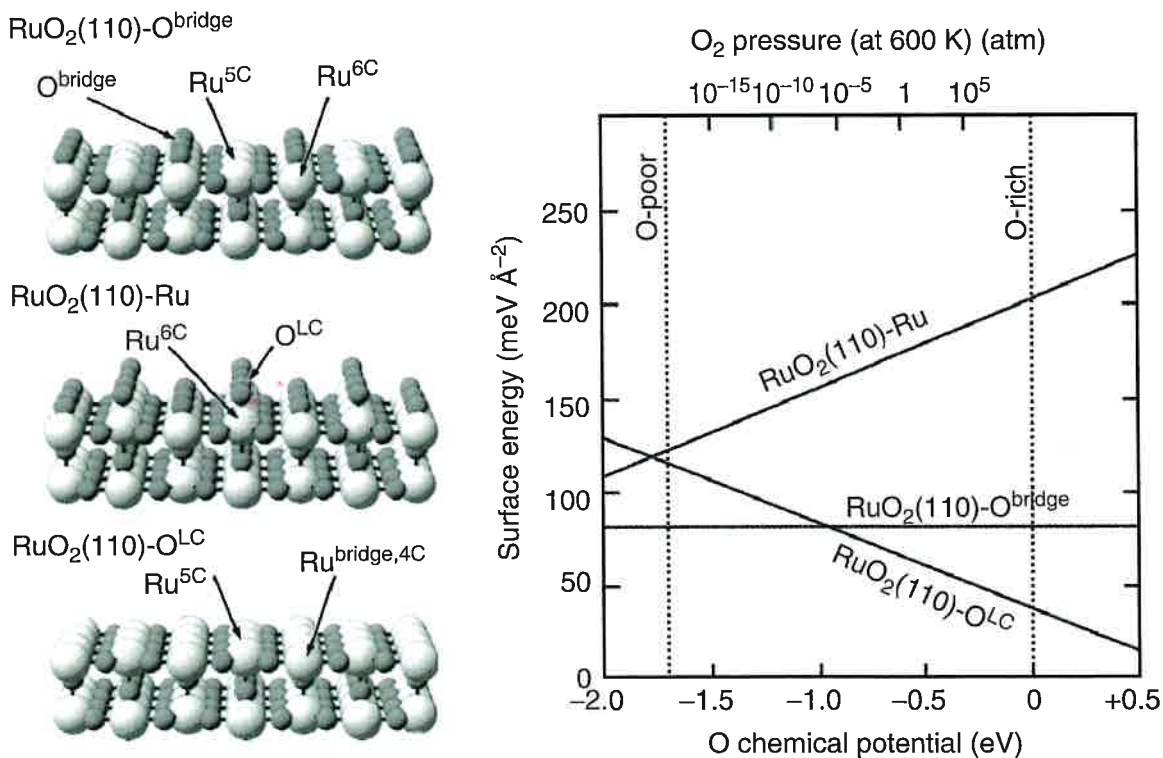


Figure 15.9 Surface phase diagram of the (110) surface of RuO_2 and the three different surface terminations; from Reuter, 2002 [21].

$\text{RuO}_2(110)\text{-O}^{\text{LC}}$. On the other hand, removing the bridging oxygen leads to exposure of the (RuO) plane, which is termed the *Ru-terminated surface*, $\text{RuO}_2(110)\text{-Ru}$. The surface free energy calculated for these three types of surfaces depending on the oxygen chemical potential $\mu(\text{O})$ is plotted in Figure 15.9. The limits “O-poor” and “O-rich” mark the points where either metal starts to evaporate from the surface or oxygen starts to condense on the surface, respectively.

Figure 15.9 shows that the $\text{RuO}_2(110)\text{-O}^{\text{bridge}}$ configuration is the most stable surface structure over a wide range of chemical potentials. However, by increasing the chemical potential above -1.0 eV , a crossover from the $\text{RuO}_2(110)\text{-O}^{\text{bridge}}$ to the fully oxygen-terminated $\text{RuO}_2(110)\text{-O}^{\text{LC}}$ termination is evident. On the top axis of Figure 15.9, the chemical potential of oxygen is converted to the oxygen partial pressure at a temperature of 600 K. At typical pressure conditions used in UHV experiments, the $\text{RuO}_2(110)\text{-O}^{\text{bridge}}$ configuration is the most stable one. However, this result shows that at oxygen partial pressures relevant for chemical reactions, the oxygen-terminated surface is the most stable one.

According to the classification of surfaces mentioned earlier, the oxygen-terminated $\text{RuO}_2(110)\text{-O}^{\text{bridge}}$ surface belongs to the unstable polar surfaces (type 3). It is, therefore, surprising that it is (under certain conditions) more stable than the stoichiometric RuO_2 surface. Actually, the stabilization of the oxygen-terminated surface is found to depend not only on the chemical potential of oxygen but also strongly on the relaxation of the surface layers, which lowers the surface energy of this polar surface to a significant extent.

Very similar concepts of surface stability criteria, as those discussed, have been described for surfaces of compound semiconductors. In this respect, the concept of autocompensation, or electron counting, has been introduced. This refers to lowering the surface energy by pairing of dangling bonds leading to completely filled anion states, and completely empty cation states, respectively. The reader is referred to Refs. [22–25].

15.2.3

Selected Examples

15.2.3.1 Rock-Salt-Type (100) and (111) Surfaces

MgO(100) and NiO(100) Magnesium oxide and nickel oxide crystallize in the rock salt structure with lattice constants of 4.21 and 4.17 Å, respectively. The (100) planes of these oxides belong to the most often studied oxide surfaces. For both types of oxides, procedures to prepare the (100) surface either by cleavage of a single crystal or by thin film growth have been reported. Figure 15.10 shows large-scale topographical as well as atomically resolved scanning probe microscopy images of the (100) surface of UHV-cleaved single crystals of MgO and NiO, respectively. Both materials are insulators with band gaps of 7.8 eV for MgO and 4.3 eV for NiO. The images of the MgO surface shown in Figure 15.10a have been obtained by noncontact atomic force microscopy (AFM) [26], whereas the NiO (Figure 15.10b) surface was imaged by scanning tunneling microscopy

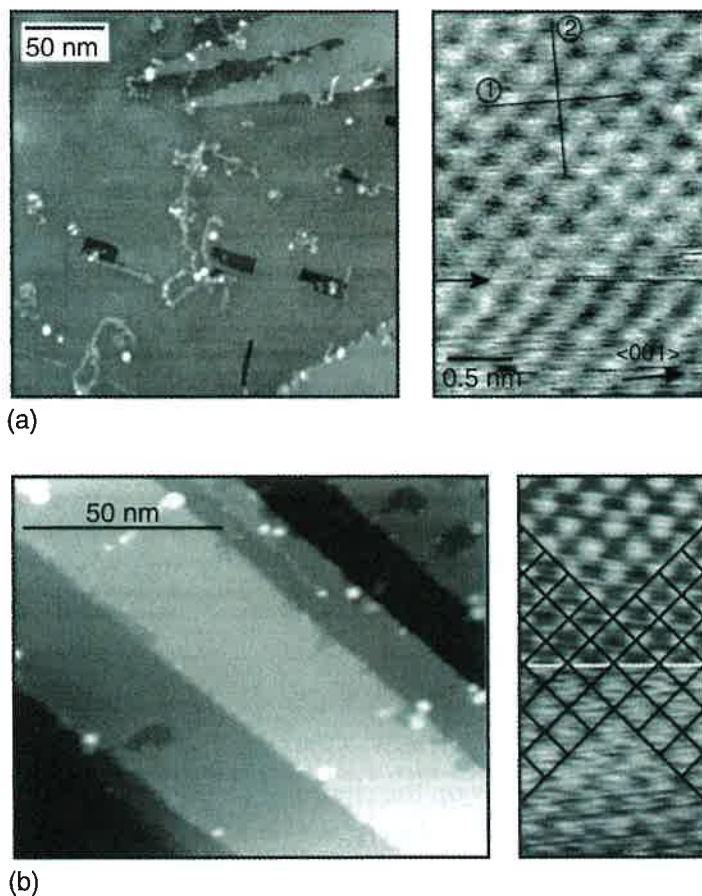


Figure 15.10 (a) Large-scale and atomically resolved AFM images of the surface of a MgO(100) single crystal; from Barth, 2003 [26]. (b) Large-scale and atomically resolved (top, positive bias; bottom, negative bias) images of the surface of a NiO(100) single crystal; from Castell, 1997 [27].

(STM) employing high temperatures, which decreases the resistivity considerably [27].

On both surfaces, relatively large (100) terraces are exposed that are separated by monoatomic steps. In the case of NiO (Figure 15.10b), the steps run predominantly along the $\langle 010 \rangle$ crystal directions, whereas on MgO, the steps appear to be more structured but are also composed of short $\langle 010 \rangle$ parts. Apart from steps, other defects that result from the cleavage process can be seen in the large-scale images, such as rectangular holes (vacancy islands) and small bright spots resulting from adatoms. Additionally, on the MgO surface, stringlike structures are visible, the exact nature of which is not clear yet.

Insights into the exact surface atomic arrangement are obtained by atomically resolved images shown in Figure 15.10. On both surfaces, an (1×1) structure of ions is observed with a distance of next-neighbor ions of about 4 Å. This value corresponds to twice the Me-O distance and thus represents the structure of either the metal or oxygen sublattice. For MgO, the chemical nature of the sublattice cannot be identified on the basis of the AFM results presented. On the other hand, for NiO, it was possible to obtain atomically resolved STM images at both positive

and negative bias (Figure 15.10b), which helped, in comparison with theoretical modeling, identify the bright spots seen at positive bias as originating from the Ni ions and those at negative bias as being oxygen ions [28].

The determination of quantitative structural parameters such as relaxation and rumpling is not possible using surface microscopy. Therefore, one needs to resort to diffraction methods for this purpose. Relaxation and rumpling effects are expected to be small on the (100) surfaces of rock salt oxides because of the very dense arrangement of surface ions and the reduction of the coordination number by only one for the (100) surface ($Z=5$) as compared to the bulk ($Z=6$). In fact, in early electron diffraction and atom scattering studies on the MgO(100) surface, only a slight inward relaxation of the first layer and a negligible rumpling was observed. There was, however, a large spread in the results, which is partly due to different surface preparation techniques. The most accurate results were obtained recently by grazing incidence X-ray scattering (GIXS) [29], medium energy ion scattering (MEIS) [30], and low-energy electron diffraction (LEED) [31] on vacuum-cleaved and -annealed surfaces that corroborated a slight inward relaxation of the first layer, which is more pronounced for the magnesium than for the oxygen ions. These results are also reproduced by calculated structural properties [32].

MgO(111) and NiO(111) The ideal bulk-terminated rock-salt-type (111) surfaces are polar surfaces terminated by a layer of only metal or only oxygen (Figure 15.11a). According to the criteria for surface stability given earlier, these surfaces are unstable and should, therefore, be subject to either structural or electronic modification. Wolf [33] predicted a stabilization of the polar rock salt (111) surfaces by a $p(2 \times 2)$ reconstruction shown in Figure 15.11b, called the *octopolar reconstruction*. This can be imagined by starting from a complete oxygen- or nickel-terminated layer, removing 25% of the ions of this layer and adding 25% of a layer of the counterions on top. This results in a pyramid-like structure as indicated in Figure 15.11b. Such a configuration fulfills the requirements of surface stability by a surface charge reduction and would, therefore, be stable. Recently, Noguera's group [34] has discussed yet another possibility going beyond the

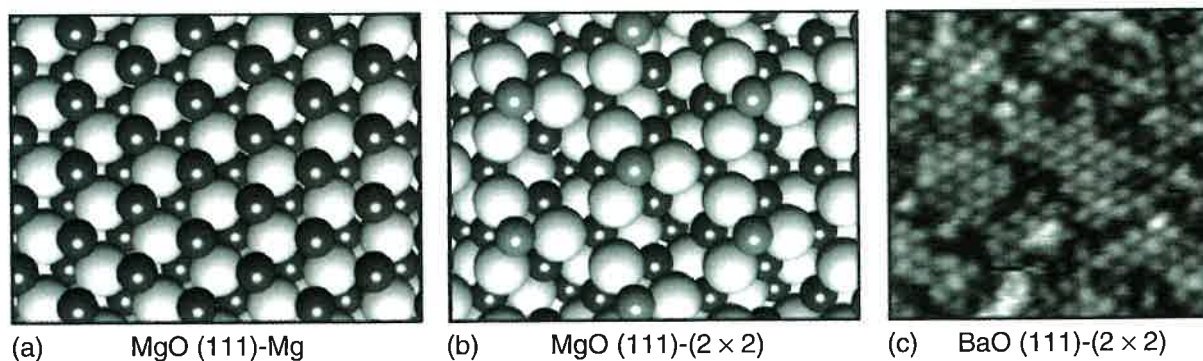


Figure 15.11 (a) Ball model of the unreconstructed rock salt (111) surface. (b) Ball model of the octopolar (2×2) reconstructed rock salt (111) surface. (c) STM image of the (2×2) reconstruction observed on BaO thin films; from Bowker, 2006 [35].

octopolar reconstruction, where in fact a mixture of surface configurations is present fulfilling both electrostatic compensation and thermodynamic equilibrium with the environment. Another possibility for stabilizing the rock salt (111) surfaces is adsorption of either OH on the metal-terminated surface or H on the oxygen-terminated (111) surface. Also in this case, the surface charge is reduced resulting in a stable surface.

The most experimental studies on polar rock-salt-type surfaces have been performed for NiO(111), on both single crystals and thin films. In early experiments on NiO(111) thin films, which were prepared by oxidation of a Ni(111) single crystal, LEED and high-resolution electron energy loss spectroscopy (HREELS) investigations indicated the presence of an OH-covered unreconstructed NiO(111) surface, which, after removing the OH groups by heating, transforms into a $p(2 \times 2)$ -reconstructed surface typical for a octopolar reconstruction, as shown in Figure 15.11b [36, 37]. The structural changes induced by adsorption and desorption of OH groups were found to be reversible but occur probably because of the high concentration of defects present on the thin film due to the large lattice mismatch between the lattices of Ni(111) and NiO(111). Better quality NiO(111) thin films could be obtained using Au(111) as substrate. The structural surface parameters obtained by GIXS on a 5 ML (monolayer) thin NiO(111) film grown on Au(111) have been compared with high-quality NiO(111) single crystals prepared by annealing in air [38]. On both surfaces, a $p(2 \times 2)$ structure, according to the theoretically proposed octopolar reconstruction, has been found to be the stable surface configuration, which showed no changes against treatment with water. Only minor relaxation of the top layers was deduced from the experimental data for both samples. However, while the single crystal exhibits a pure Ni termination, both oxygen and nickel terminations are present on the thin film. The stability of the octopolar $p(2 \times 2)$ reconstruction is very sensitive to the environmental conditions, as annealing of NiO(111) $p(2 \times 2)$ under UHV conditions leads to reduction and the formation of Ni clusters on the surface [39]. Microscopic evidence for the presence of an octopolar reconstruction comes from STM studies conducted on very thin (2–3 ML) NiO(111) films grown on Au(111) [40, 41]. Only recently, an STM study of thin BaO(111) films grown on Pt(111) revealed also an octopolar reconstruction that is evident from the hexagonal surface pattern shown in Figure 15.11c [35].

While air annealing of NiO(111) single crystals is an appropriate way to stabilize the $p(2 \times 2)$ reconstruction with Ni termination, similar sample preparation of MgO(111) single crystals yields a (1×1) structure that results from an unreconstructed, O-terminated (111) surface covered by hydrogen [42]. On annealing of MgO(111) single crystals to above 1450 °C, partial reduction and the occurrence of a $(\sqrt{30} \times \sqrt{30})R30^\circ$, a (2×2) , and a $(2\sqrt{30} \times 2\sqrt{30})R30^\circ$ structure was observed.

Finally, it should be mentioned that attempts to prepare thin MgO(111) films on Ag(111) by alternating deposition of magnesium and oxygen resulted in unreconstructed MgO(111) layers that show semiconducting or even metallic behavior [43, 44].

15.2.3.2 Corundum-Type Surfaces – Al_2O_3 , Cr_2O_3 , Fe_2O_3 , V_2O_3

The most thoroughly studied surface structures of corundum-type oxides are those of the (0001) planes of Al_2O_3 , Cr_2O_3 , Fe_2O_3 , and V_2O_3 . In the hexagonal unit cell, the oxygen ions form close-packed hcp layers with the metal ions occupying two-thirds of the octahedral interstitial sites. Owing to the presence of vacant octahedral sites in the lattice, the metal ions have a slightly distorted octahedral environment leading to a stacking sequence along the [0001] direction of $-\text{Al}-\text{O}_3-\text{Al}-\text{Al}-\text{O}_3-\text{Al}-$, as schematically shown in Figure 15.12. Three different ideal bulk terminations can be obtained in the [0001] direction: cutting the crystal between the upper Me and O_3 layer results in the double metal layer (0001)-2Me surface, separating the crystal between the two metal layers results in the single metal layer (0001)-Me surfaces, and the oxygen-terminated (0001)-O surface (Figure 15.12). From electrostatic considerations, only the single metal layer (0001)-Me surface, as a “type 2” surface, is charge neutral and expected to be stable, whereas the other two configurations are “type 3” surfaces with a diverging electrostatic energy. On the (0001)-Me surface, the cation coordination is reduced from 6 (octahedral) in the bulk to 3 on the surface. For such a coordinative unsaturation, a strong relaxation of the first layers is to be expected.

Structural investigations of $\alpha\text{-Al}_2\text{O}_3(0001)$ single-crystal samples have been performed using GIXS [13] and LEED [45]. In both cases, the stable surface structure that results from annealing the sample to about 1000 K is the single Al-layer-terminated structure represented in the middle of Figure 15.12. A strong vertical relaxation of the first layers was found, which was confirmed by calculations [46, 47], whereas in the surface plane, only small deviations from the bulk-terminated structure appear (Figure 15.13b). The stability of the $\text{Al}_2\text{O}_3(0001)\text{-Al}$ surface is also evidenced by the calculated surface phase diagram shown in Figure 15.13a [46, 47]. Under all allowed ranges of the oxygen chemical potential, the $\text{Al}_2\text{O}_3(0001)\text{-Al}$ phase exhibits a lower surface energy as compared to the polar (0001)-2Me and (0001)-O phases. Annealing of $\text{Al}_2\text{O}_3(0001)$

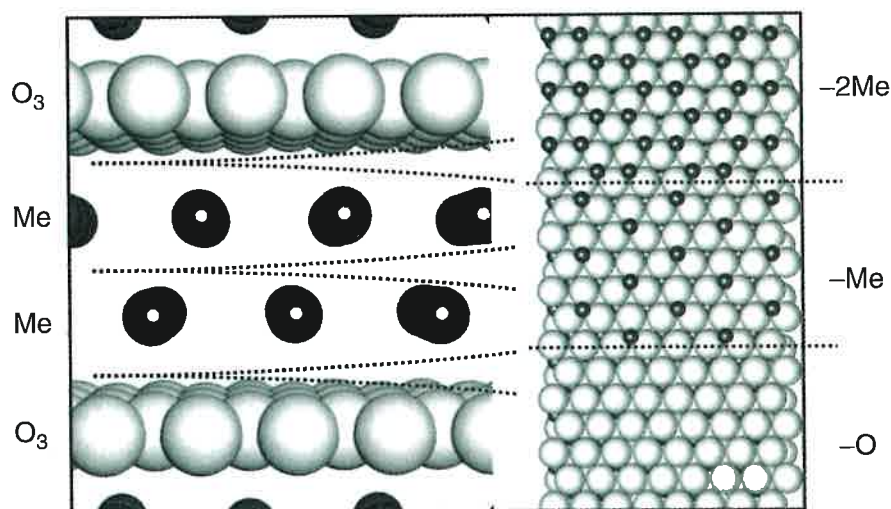


Figure 15.12 Cutting planes and corresponding surface terminations of the corundum (0001) surface.

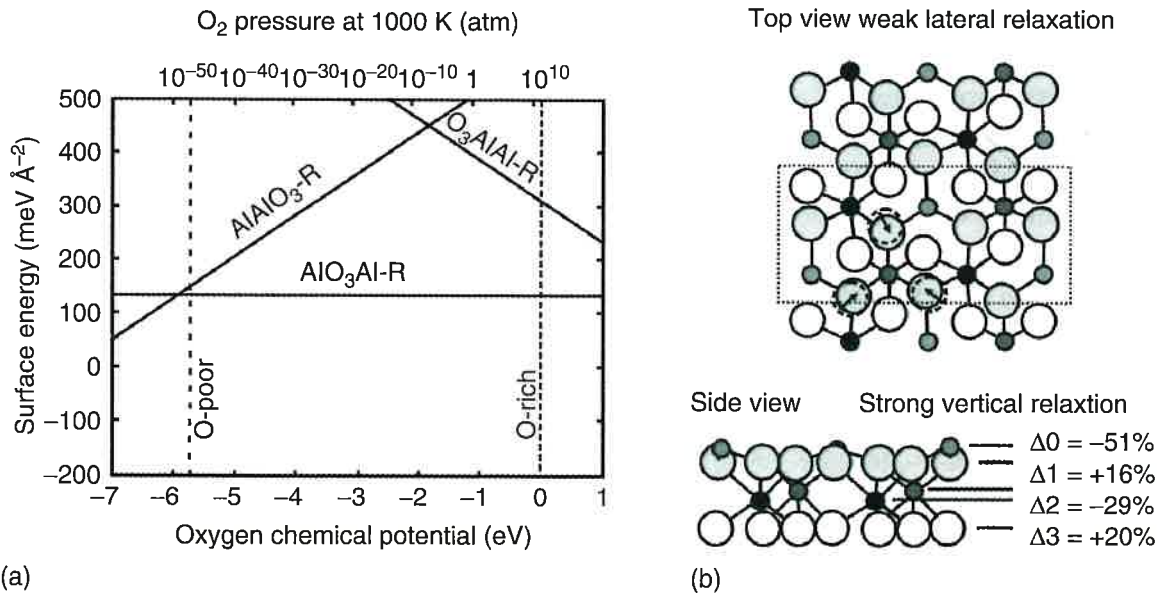


Figure 15.13 (a) Calculated surface phase diagram of the Al₂O₃(0001) surface; from Batyrev, 1999 [46]. (b) Model of the relaxed Al₂O₃(0001) surface according to GIXS measurements; from Renauld, 1998 [13].

to temperatures above 1300 K leads to partial reduction of the surface and the observation of other regular surface structures including (2×2) , $(3\sqrt{3} \times 3\sqrt{3})R30^\circ$, and $(\sqrt{31} \times \sqrt{31})R\pm 9^\circ$ [48].

Although there is some ambiguity on whether the single-crystal Al₂O₃(0001) surfaces are covered by hydrogen or not, the surface structure of well-prepared Al₂O₃(0001) single crystals is experimentally well described and represents a strongly relaxed, but bulk-terminated surface. The situation is different for thin film samples, where a detailed surface structure determination turned out to be rather difficult. Alumina thin films have been prepared on different substrates including NiAl(110) [49, 50], Ni₃Al(111) [51], Mo(110) [52], and Ta(110) [53]. By far the most experimental studies have been performed on the alumina/NiAl(110) thin film, which is prepared by oxidation of the NiAl(110) surface at high temperature. Only recently, the structure of the film, the thickness of which is restricted to two layers by a self-limiting growth, has been determined by a combination of STM experiments and density functional theory (DFT) calculations (Figure 15.14a) [54]. The stoichiometry is Al₁₀O₁₃ with a stacking sequence 4(Al₄O₆Al₆O₇). The surface layer of this film consists of almost coplanar aluminum and oxygen layers, where the ions in the oxygen layer are arranged squarelike and the aluminum ions are ordered nearly hexagonal. For the surface Al ions, both tetrahedral and square-pyramidal coordination are found, a configuration that may also be present at the reconstructed $(\sqrt{31} \times \sqrt{31})$ Al₂O₃(0001) surface mentioned earlier. The most common defects on this surface are domain boundaries as shown in Figure 15.14b, which considerably influence the nucleation of metal clusters on this thin film [55].

In early experiments on Cr₂O₃(0001) thin films, a single-layer metal termination as in the case of Al₂O₃(0001) single crystals was found. From the corresponding

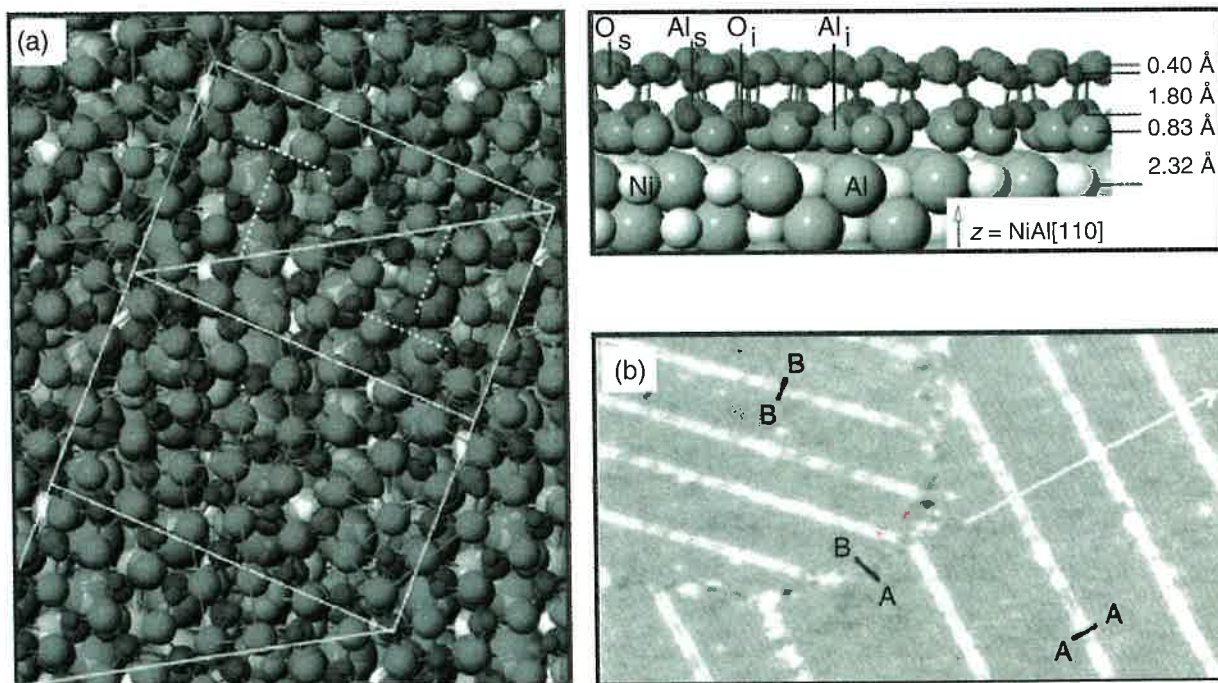


Figure 15.14 (a) Surface structure of a thin alumina film grown on NiAl(110); from Kresse, 2005 [54]. (b) STM image of a thin alumina film grown on NiAl(110) showing antiphase domain boundaries; from Bäumer, 1999 [55].

(1×1) LEED pattern, which shows a diffuse background, it was concluded that already at room temperature, the diffusion of chromium ions is high, which leads to a statistical occupancy of various surface sites. The conclusion was corroborated by subsequent X-ray diffraction measurements on $\text{Cr}_2\text{O}_3(0001)$ single crystals [56] as well as from STM measurements on $\text{Cr}_2\text{O}_3(0001)$ thin films [57].

Stoichiometric and single-layer vanadium-terminated single-crystal $\text{V}_2\text{O}_3(0001)$ surfaces were prepared by annealing V_2O_3 single crystals in oxygen atmosphere [58]. More complex surface structures appear on the $\text{Fe}_2\text{O}_3(0001)$ surface during *in situ* preparation under UHV conditions depending on annealing temperature and oxygen partial pressure. Combined LEED and X-ray photoelectron spectroscopic (XPS) measurements revealed that the $\text{Fe}_2\text{O}_3(0001)$ surface is terminated by a $\text{Fe}_3\text{O}_4(111)$ layer after annealing up to 775°C , which transforms into a mixed $\text{Fe}_{(1-x)}\text{O}/\text{Fe}_2\text{O}_3$ structure at slightly higher temperature. A (1×1) LEED pattern corresponding to a bulk-terminated $\text{Fe}_2\text{O}_3(0001)$ surface was only observed after heating at 900°C in 1×10^{-6} mbar O_2 [59]. In subsequent studies, the evolution of the different surface phases of $\text{Fe}_2\text{O}_3(0001)$ single crystals was examined with STM. Thornton and coworkers succeeded in imaging both the $\text{Fe}_3\text{O}_4(111)$ -terminated surface obtained by annealing a $\text{Fe}_2\text{O}_3(0001)$ single crystal to 730°C at 1×10^{-6} mbar O_2 [60], as well as a mixed $\text{FeO}/\text{Fe}_2\text{O}_3$ layer after annealing in oxygen to 800°C [61]. Different to the conclusion drawn from the LEED results suggesting that FeO forms an overlayer on Fe_2O_3 , the STM results clearly show a coexistence of the two phases with long range order, which was termed *biphase ordering* (Figure 15.15).

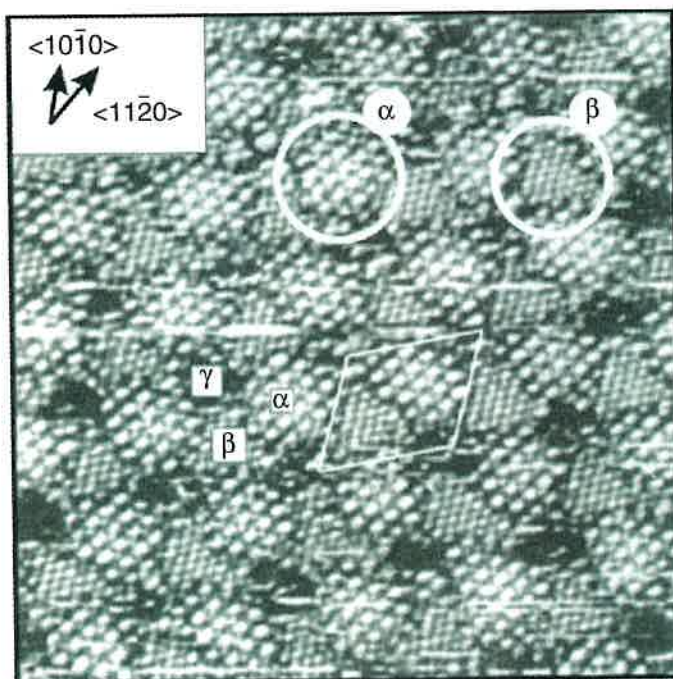


Figure 15.15 STM image ($20 \times 20 \text{ nm}^2$) of the surface of $\text{Fe}_2\text{O}_3(0001)$ showing biphase ordering of coexisting FeO (α) and Fe_2O_3 (β) phases; from Condon, 1995 [61].

The dependence of the surface structure of the $\text{Fe}_2\text{O}_3(0001)$ surface on the oxygen partial pressure has been investigated for $\text{Fe}_2\text{O}_3(0001)$ thin films grown on $\text{Pt}(111)$. For this purpose, an initially grown $\text{Fe}_3\text{O}_4(111)$ film was oxidized at constant temperature (830°C) at varying oxygen partial pressures (for preparation of FeO films see [62, 63]). In Figure 15.16a–e, a series of STM images obtained after different stages of oxidation is presented [64]. At high oxygen partial pressure (Figure 15.16a), the surface is terminated almost completely by the phase termed “B.” Small patches of a surface phase “A” are apparent in this image, which, with less oxygen present during preparation (Figures 15.16b–d), becomes more abundant. Finally, at an oxygen partial pressure of 10^{-5} mbar, phase “A” becomes the only existing surface termination. Further decrease of $p(\text{O}_2)$ during annealing results in reduction of the surface and also the appearance of the biphase ordering on single-crystal $\text{Fe}_2\text{O}_3(0001)$. A distinction between surface terminations A and B was possible on the basis of different step heights between adjacent terraces of the same (B-B) and different (B-A) termination, respectively, as indicated by the line profile shown in Figure 15.16b. For both surface terminations, identical LEED (1×1) patterns were observed.

According to the surface phase diagram presented in Figure 15.16f for the three common Fe_2O_3 bulk terminations ([65]; in the original paper, additional terminations have also been considered), which shows increased stability of the oxygen terminated over the single-layer iron-terminated $\text{Fe}_2\text{O}_3(0001)$ surface at high oxygen chemical potentials, the STM data have been interpreted as arising from $-\text{Fe}-\text{Fe}-\text{O}_3$ termination after treatment at high oxygen partial pressure (Figure 15.16a), which gradually transforms into the $-\text{Fe}-\text{O}_3-\text{Fe}$ surface (Figure 15.16e) when the

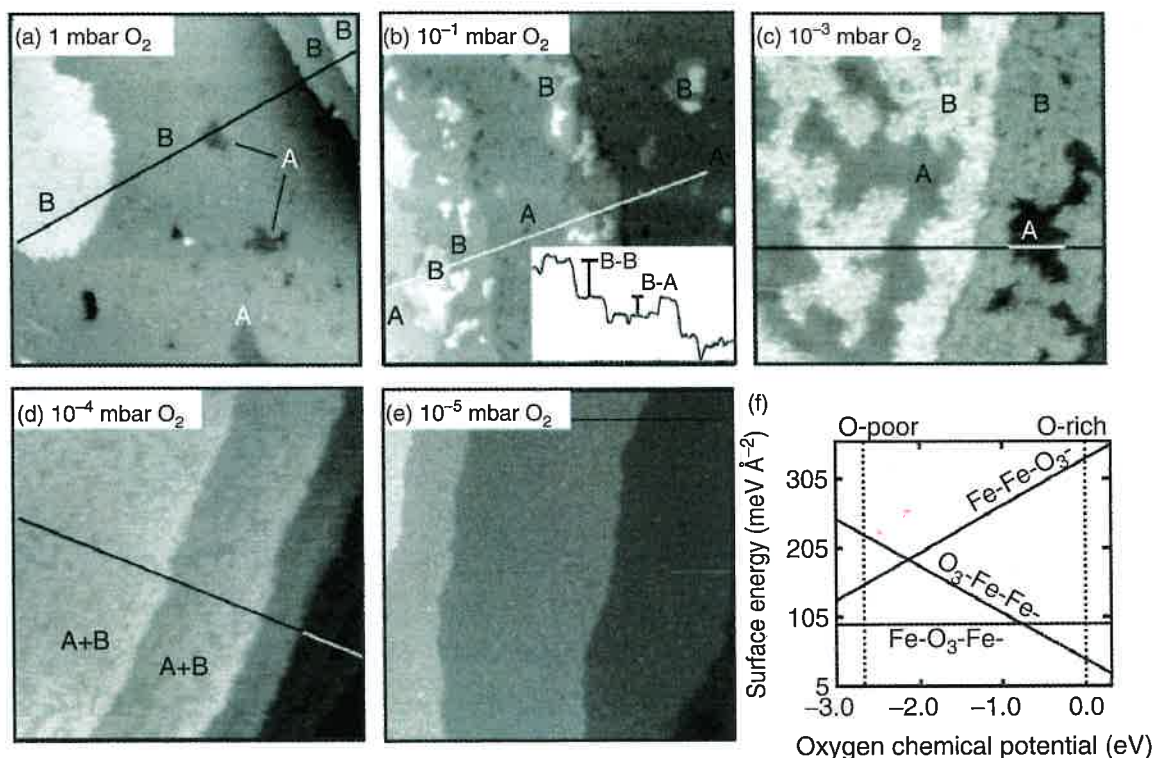


Figure 15.16 (a–e) STM images of Fe₂O₃(0001) thin films depending on the oxygen partial pressure during preparation; from Shaikhutdinov, 1999 [64]. (f) Surface phase diagram of Fe₂O₃(0001); from Wang, 1998 [65].

oxygen pressure in the reservoir is reduced. It turned out, however, that this interpretation is only partly correct. In subsequent experimental and theoretical studies, a surface structure that was not considered before was identified that gave rise to surface termination at high oxygen partial pressure. This structure arises from single oxygen atoms double-bonded to the metal ions of a single-layer iron-terminated surface, resulting in ferryl (Fe=O) groups. Figure 15.17a shows a (30 × 30) nm² STM image of a Fe₂O₃(0001) surface prepared by oxidation of Fe₃O₄(111) at 10⁻² mbar O₂ and 1040 K. The atomically resolved image taken on a flat area shown in the inset of Figure 15.17a shows a hexagonal structure with a periodicity of about 5 Å. Evidence for the presence of ferryl groups comes from a vibrational spectrum (Figure 15.17b) taken from a surface prepared with the same recipe as in the case of the STM experiment, which shows a band at 989 cm⁻¹ that could unambiguously be assigned as arising from the Fe₂O₃(0001) surface [66]. Additional proof for this assignment comes from calculated surface phase diagrams where the ferryl termination is also considered. In Figure 15.17c, the stability of different Fe₂O₃(0001) surface structures depending on the temperature at an oxygen equilibrium pressure of 0.2 mbar is presented [67], which shows that the ferryl termination (-Fe-O₃-Fe-O) represents a stable surface structure that separates the limiting cases of the fully oxygen-covered (Fe-Fe-O₃) and stoichiometric (-Fe-O₃-Fe) terminations. A further theoretical study has shown that by incorporation of correlation effects, the stability of the fully oxygen-terminated surface is disfavored in the whole region of allowed oxygen chemical potentials and only the metal and

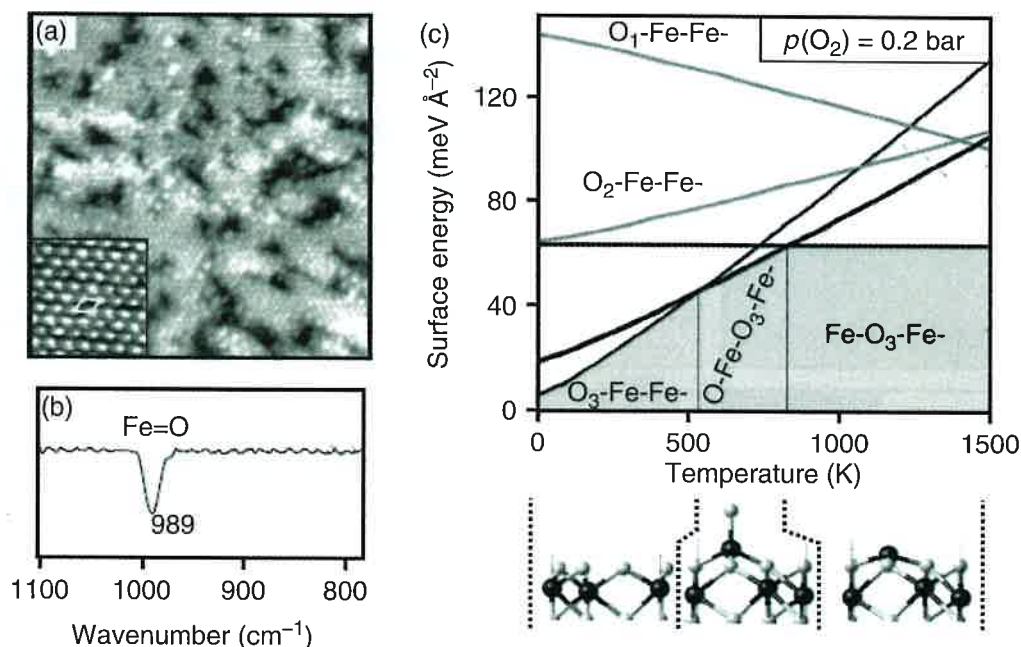


Figure 15.17 (a) STM image ($30 \times 30 \text{ nm}^2$) of a ferryl-terminated $\text{Fe}_2\text{O}_3(0001)$ surface and (b) IRAS spectrum showing an infrared band due to surface ferryl groups; from Lemire, 2005 [66]. (c) Surface phase diagram of the $\text{Fe}_2\text{O}_3(0001)$ surface including the ferryl-terminated surface; from Bergermeyer, 2004 [67].

ferryl terminations are stable surface structures [68]. Coming back to Figure 15.16, the structural changes observed by varying the oxygen partial pressure during preparation on $\text{Fe}_2\text{O}_3(0001)$ thin films arise from a transformation of a ferryl-terminated to a metal-terminated surface. It has to be noted that for $\text{Fe}_2\text{O}_3(0001)$ films grown in a different way, that is, by oxygen plasma-assisted molecular beam epitaxy on $\text{Al}_2\text{O}_3(0001)$ substrates, despite the high oxygen concentration during growth, a metal-terminated surface was observed [69, 70].

The termination of $\text{Fe}_2\text{O}_3(0001)$ by ferryl groups is not the only example where a surface structure containing $\text{Me}=\text{O}$ groups is found. In fact, on other corundum-type (0001) surfaces, the formation of such groups has also been observed. Adsorption of O_2 on metal-terminated $\text{Cr}_2\text{O}_3(0001)$ thin films leads to the formation of chromyl groups ($\text{Cr}=\text{O}$) that are stable up to 600 K [71]. An STM and HREELS study on the growth of up to 3 ML thin $\text{V}_2\text{O}_3(0001)$ films on $\text{Pd}(111)$ [72] and $\text{Rh}(111)$ [73] has shown that under the preparation conditions applied, the vanadyl ($\text{V}=\text{O}$)-terminated surface is the stable surface structure of these thin films. The same conclusion has been drawn from similar studies on thicker $\text{V}_2\text{O}_3(0001)$ films grown on $\text{W}(110)$ and $\text{Au}(111)$ [74]. The vanadyl groups are more stable than chromyl groups and the terminating oxygen can be removed thermally only after heating up to 1000 K, which also leads to diffusion of W from the substrate to the surface and, consequently, to an irreversible change of the surface properties. Another way to reduce the vanadyl-terminated surface to form a metal-terminated $\text{V}_2\text{O}_3(0001)$ surface is by electron bombardment. In Figure 15.18a, an STM image obtained from the vanadyl-terminated $\text{V}_2\text{O}_3(0001)$ surface, revealing the hexagonal structure of this surface is shown [75]. This surface can be stepwise-reduced to

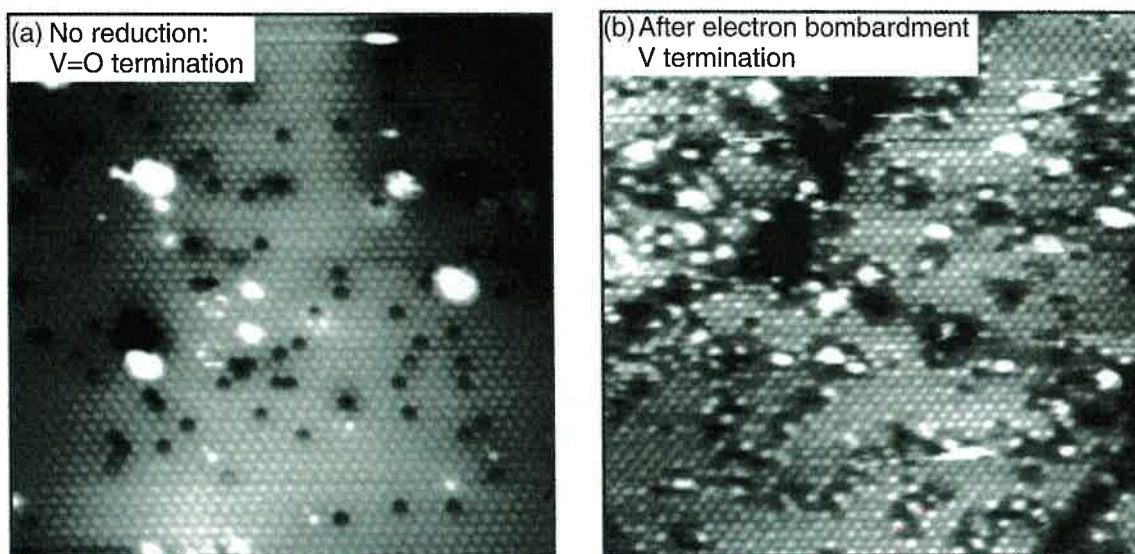


Figure 15.18 STM images ($20 \times 20 \text{ nm}^2$) of the vanadyl-terminated (a) and metal-terminated (b) surface of $\text{V}_2\text{O}_3(0001)$ thin films; from Guimond, 2006 [75].

obtain a metal-terminated surface, which can be identified, although the lattice parameters are the same as for the vanadyl-terminated surface, by the different appearance in STM (Figure 15.18b).

15.2.3.3 Wurtzite Structure

The most prominent and exclusively studied representative oxide crystallizing in the wurtzite structure is ZnO. In wurtzite, the cations and anions are tetrahedrally coordinated and hexagonally stacked along the c -axis as shown in Figure 15.2. Four low-index surface planes are important: the nonpolar $(10\text{--}10)$ and $(11\text{--}20)$ surfaces and the polar (0001) and $(000\text{--}1)$ surfaces. The $(10\text{--}10)$ surface contains one Zn-O dimer that is aligned in rows along the $[1\text{--}210]$ direction. On the $(11\text{--}20)$ surface, two Zn-O dimers form zigzag lines on the surface. The polar surfaces are created by cleavage of a crystal normal to the c -axis between an oxygen and a zinc layer. In this way, two different surface terminations are derived, where one contains only Zn ions (the (0001) -Zn surface) and the other one contains only O ions (the $(000\text{--}1)$ -O surface).

Nonpolar Surfaces The $(10\text{--}10)$ and $(11\text{--}20)$ surfaces of ZnO expose the same amount of cations and anions and are, therefore, stoichiometric and nonpolar. STM images of both the $(10\text{--}10)$ and $(11\text{--}20)$ surfaces are shown in Figure 15.19 and Figure 15.20, respectively ([76, 77], see also [78]). The $(10\text{--}10)$ surface shows flat terraces separated by monoatomic steps that run along the $[0001]$ or $[-12\text{--}10]$ direction (Figure 15.19a). On the other hand, the surface morphology of the $(11\text{--}20)$ face is rougher, which was initially connected to the lower stability of this face. Atomic resolution could be obtained on either surface (Figure 15.19b and Figure 15.20b, respectively) by STM at positive bias. Under these conditions, metal ions are usually imaged by STM on oxide surfaces. The structure of the

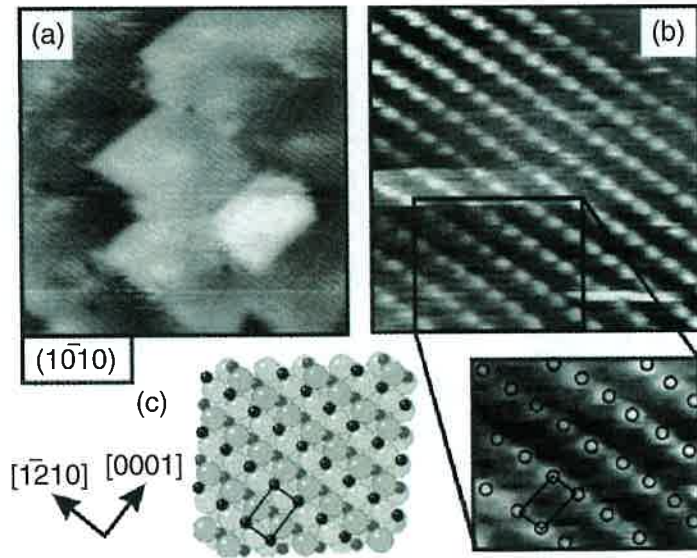


Figure 15.19 (a) Large-scale ($50 \times 50 \text{ nm}^2$) and (b) atomically resolved ($5 \times 5 \text{ nm}^2$) STM image of the $\text{ZnO}(10\bar{1}0)$ surface. (c) Atomic model of the bulk-terminated $\text{ZnO}(10\bar{1}0)$ surface; from Diebold, 2004 [77].

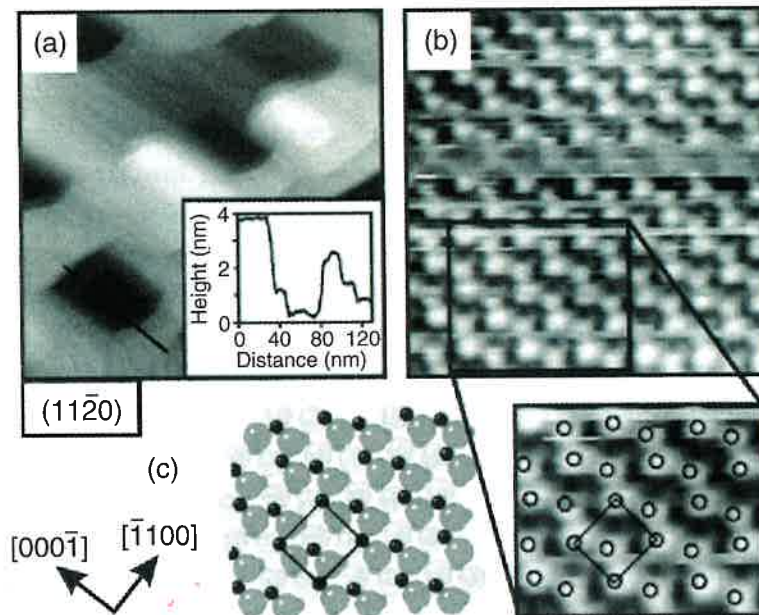


Figure 15.20 (a) Large-scale ($200 \times 200 \text{ nm}^2$) and (b) atomically resolved ($5 \times 5 \text{ nm}^2$) STM image of the $\text{ZnO}(11\bar{2}0)$ surface. (c) Atomic model of the bulk-terminated $\text{ZnO}(11\bar{2}0)$ surface; from Diebold, 2004 [77].

atomic contrast perfectly reproduces the atomic arrangement of the bulk-truncated surfaces (Figure 15.19c and Figure 15.20c).

The relaxation of the outermost surface layer on the $(10\bar{1}0)$ surface has been determined in an early LEED experiment to be larger for the Zn ions than that for the O ions, the values being $\Delta d(\text{Zn}) = -0.45 \text{ \AA}$ and $\Delta d(\text{O}) = -0.05 \text{ \AA}$, respectively, which leads to a tilting of the Zn-O surface dimer of 12° [79]. This result has been confirmed by angle-resolved ultraviolet photoelectron spectroscopic (UPS)

measurements [80]; however, in a more recent GIXS study [81], almost no relaxation was observed. There has also been some discrepancy in the amount of the first-layer relaxation with various theoretical approaches [82–87]. In a recent theoretical study using first-principles DFT [88], a large inward relaxation on the (10–10) surface of $\Delta d(\text{Zn}) = -0.36 \text{ \AA}$ and $\Delta d(\text{O}) = -0.04 \text{ \AA}$ was obtained, confirming the result of the previous LEED study. A similar relaxation was obtained for the (11–20) surface.

Polar ZnO Surfaces The polar surfaces of ZnO are the so-called Tasker type 3 (Section 15.2.2) surfaces constituting alternating layers of oppositely charged ions. In the purely ionic model, the stabilization of these polar surfaces is achieved via a charge redistribution that increases the formal charge of Zn ions on the Zn-terminated surface from +2 to +3/2 and reduces the formal charge of O ions on the O-terminated surface from –2 to –3/2. The charge compensation can be achieved by electron transfer from the O- to the Zn-terminated surface, by removing surface ions, or by adsorption of charged species.

Early experimental studies of the polar ZnO surfaces using diffraction methods gave exclusively (1×1) diffraction patterns implying that clean, bulk-truncated polar surfaces of ZnO are stable under UHV conditions. Therefore, a charge transfer from the O- to the Zn-terminated face was proposed to be the dominating mechanism for stabilization of the polar surfaces. This mechanism leads to partially occupied bands, and thus the metallic behavior of the surface [89]. However, such occupied surface states have never been observed experimentally by angle-resolved photoemission [80, 90]. It is, therefore, questionable, whether the surface stabilization by metallization is indeed the acting force or other mechanisms such as reconstruction or adsorption of hydroxyl groups are more favorable. Recent STM studies carried out in the groups of Diebold and Thornton [76–78, 91] have shed more light onto this discrepancy. Figure 15.21 shows STM images taken from the (0001)-Zn (Figure 15.21a) and (000–1)-O surfaces (Figure 15.21c). The Zn-terminated surface (Figure 15.21a) exhibits a high density of irregular distributed triangular holes and added islands with characteristic shape and monoatomic step height. This surface also gives rise to a (1×1)

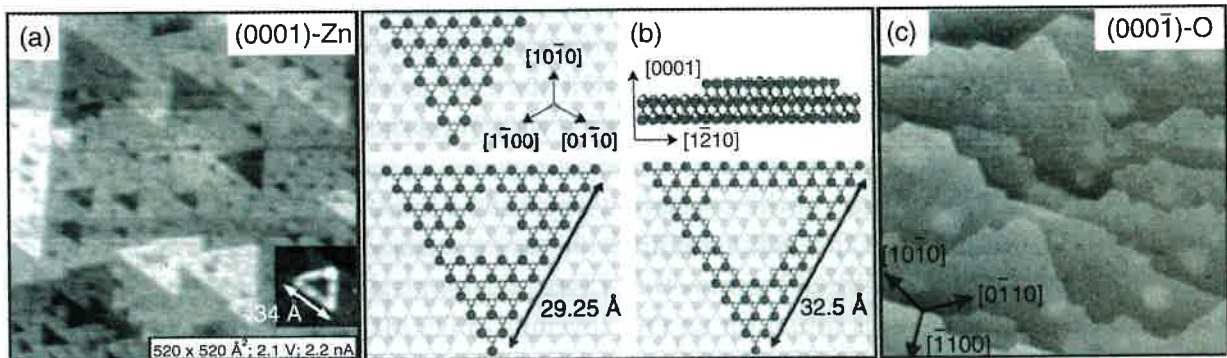


Figure 15.21 (a) STM image of the metal-terminated ZnO(0001)-Zn surface. (b) Atomic model for triangular features observed on this surface; from Dulub, 2002 [76], Kresse, 2003 [89]. (c) STM image of the oxygen-terminated ZnO(000–1) surface; from Diebold, 2004 [77].

LEED pattern; however, scanning tunneling spectroscopy (STS) data did not give any evidence for a surface state, which rules out metallization by charge transfer and makes a charge compensation mechanism involving reconstruction most plausible. In order to account for the observed structures, an atomic model as shown in Figure 15.21b has been constructed with the step edges of the triangles terminated by oxygen ions. Such structures would account for canceling the surface charge by removing one-fourth of the Zn ions from the surface.

On the other hand, the O-terminated surface shows smooth terraces with no visible reconstruction (Figure 15.21c). Contrary to the Zn-terminated surface, the step edges are diatomic in height and, therefore, stoichiometric. Also in the case of the O-terminated surface, no evidence for surface metallization was found by STS. The authors explained their observation of smooth terraces by stabilization of the polar surface due to adsorption of residual hydrogen. There has been a controversial discussion in the literature whether or not an unreconstructed O-terminated surface can be prepared in UHV. Helium atom scattering and LEED experiments have shown that a freshly annealed (000-1)-O surface gives rise to a (1×3) diffraction pattern, which was ascribed to an ordered alignment of oxygen vacancies, whereas a (1×1) pattern arises only from a hydroxyl-covered surface [92]. In a subsequent study, it was argued that although a small amount of hydroxyl groups (0.05 ML) was detected with HREELS, the observed (1×1) LEED pattern stems from an unreconstructed (000-1)-O surface [93]. Clearly, the nature of the polar ZnO surfaces strongly depends on the preparation conditions. Therefore, in the following, the results of recent calculations concerning the stability of the polar ZnO surfaces under different environmental conditions will be discussed.

Stabilization of the (0001)-Zn Surface On the basis of the STM observation of triangular pits and islands on the (0001)-Zn surface, extensive DFT calculations have been carried out for this surface to elucidate different stabilization mechanisms [89]. In this study, the stabilization of the (0001)-Zn surface by adsorption of OH groups or O adatoms, and by formation of single Zn vacancies and triangular pits as observed by STM, has been elucidated and compared to the ideal bulk-truncated (0001)-Zn surface. The results are summarized in the surface phase diagram shown in Figure 15.22a. On the bulk-truncated surface, a Zn-derived surface state is filled by 0.5 electrons. It was found that all of the above-mentioned stabilization mechanisms can account for canceling the extra charge and lead to an effective reduction of the surface energy, thus a more stable surface morphology, as compared to the bulk-truncated (0001)-Zn surface. At H-rich conditions, the surface covered by OH groups is the thermodynamically most stable. The minimal surface energy is found for an OH coverage of 0.5 ML, which corresponds exactly to the amount of OH groups that is necessary to cancel the Zn surface state. Under H-poor conditions, a surface exhibiting triangular reconstructions as observed with STM is the most stable morphology. Depending on the oxygen chemical potential, the different structures are stable. It could be shown that the triangular structures

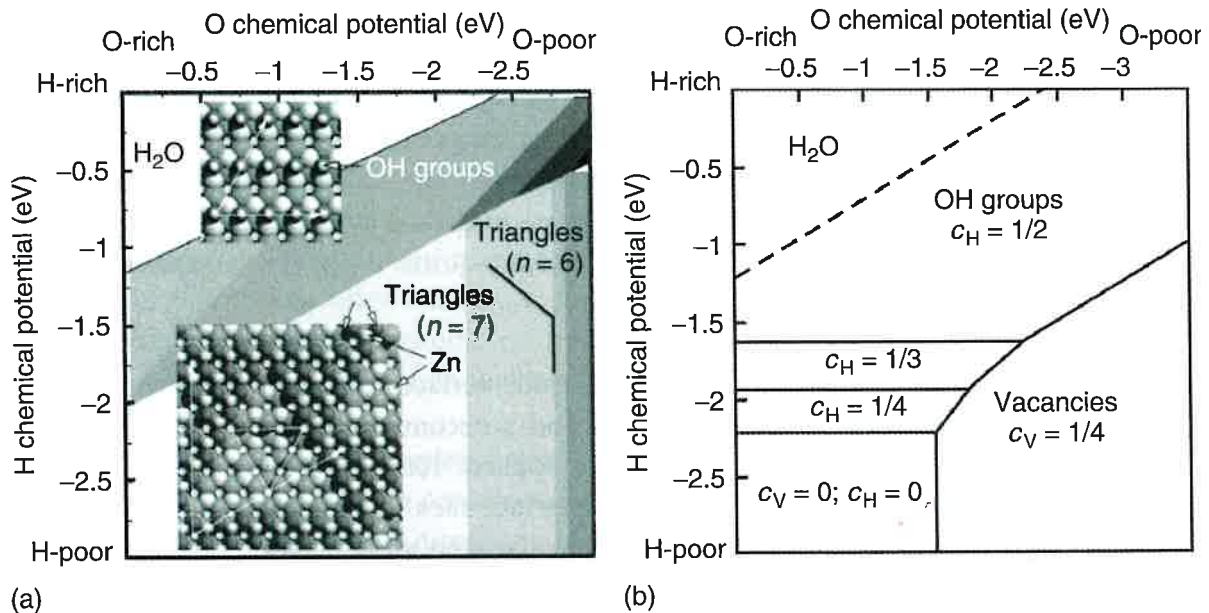


Figure 15.22 (a) Surface phase diagram of the metal-terminated ZnO(0001)-Zn surface with stability regions for the triangular features observed with STM from Kresse, 2003 [89]. (b) Surface phase diagram of the oxygen-terminated ZnO(000-1)-O surface depending on both oxygen and hydrogen chemical potentials; from Meyer, 2004 [94].

are more stable than single Zn vacancies and that larger triangular islands are preferred over small ones.

An important fact is that the surface hydroxylation as well as the adsorption of O atoms almost completely lifts the relaxation inside the first double layer, which, for the bulk-truncated surface, amounts to 33% of the bulk interlayer distance. It should be noted that in most experimental studies, a slight outward relaxation of a small percentage of the interlayer distance has been determined [95–97], and only recently, an inward relaxation of the Zn-terminated surface, as predicted by calculations, was observed experimentally [98].

Stabilization of the (000-1)-O Surface Similar calculations have been performed for the (000-1)-O surface. The surface phase diagram of the O-terminated surface in thermal equilibrium with hydrogen and oxygen is shown in Figure 15.22b [94]. Hydroxyl groups are stable on the O-terminated surface for a wide range of temperatures and H₂ partial pressures. Increasing the temperature partially removes the hydroxyl groups and finally, oxygen vacancies are created.

Again, as in the case of the Zn-terminated surface, also on the O-terminated surface, the formation of OH groups completely lifts the surface relaxation, which for the bulk-truncated surface was calculated to be almost half of the interlayer distance [99, 100].

15.2.3.4 Defects on Oxide Surfaces

So far we have restricted our discussion on oxide surfaces to the geometry of terraces. However, any description of surface properties has to include defects,

as those are often the sites of chemical activity. Surfaces prepared either by cleavage of single crystals or by epitaxial growth of thin films always contain a variety of defects. The most obvious seen with microscopic techniques are steps separating two terraces. Point defects such as ion vacancies are always present in the bulk of oxide crystals at finite temperature. Their identification on the surface is a somewhat different task, because point defects are considered as the most reactive sites on clean oxide surfaces, which requires very clean conditions to study them.

Steps For the formation of steps on oxide surfaces and their stability, the same concepts, namely, charge neutrality and autocompensation, as applied for the stability of regular surfaces, may be applied. Ions exposed at step sites have lower coordination than the respective terrace sites. The coordinative unsaturation leads also to slight structural relaxation at step sites. Experimentally, the step direction can be measured by quantitative $I-V$ LEED, or may be inferred from microscopic data, where the principal crystal directions are directly seen. However, with the complexity of crystal structures that are possible for oxide surfaces, the determination of step structures is not straightforward.

For the simplest case of a rock salt oxide such as MgO, where the (100) surface is by far the most stable surface, the minimum energy step orientation is also [100]. This step orientation is the most common observed experimentally, for example, in Figure 15.23a for MgO thin films. In this case, the steps are composed of an alternating arrangement of 4-coordinated magnesium and oxygen ions, which do not lead to formation of a dipole moment on the surface. The step height amounts to 2.1 Å, which corresponds to one-half of the lattice constant, that is, a

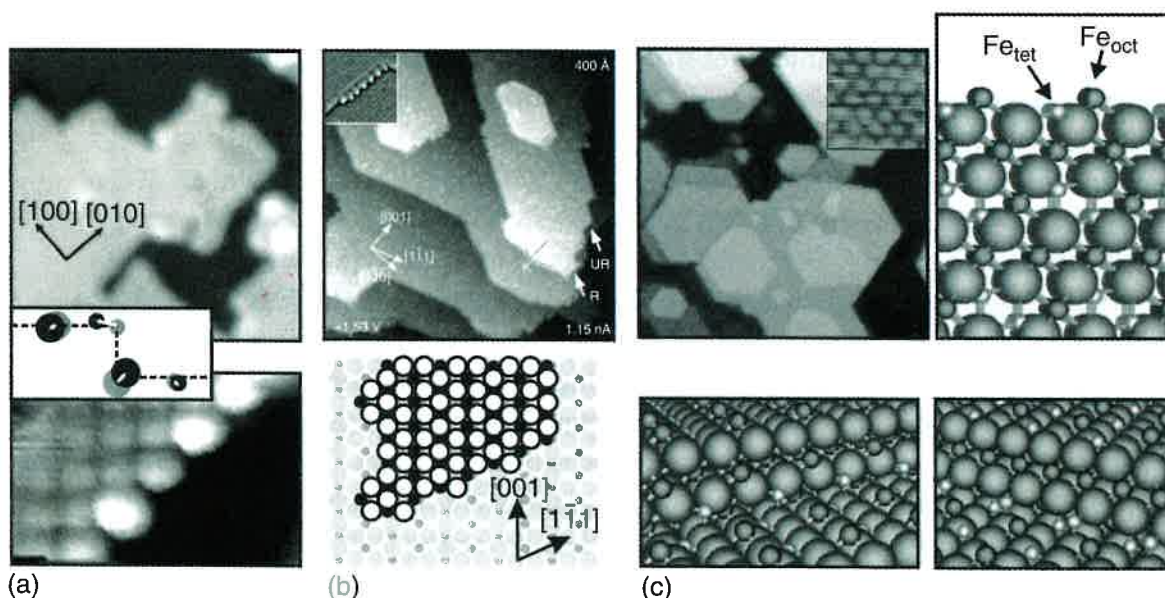


Figure 15.23 Upper panel: large-scale STM images of (a) MgO(001) thin films (Sterrer, M. and Freund, H.-J., unpublished), (b) TiO₂(110) (from Diebold, 1998 [104]), and (c) Fe₃O₄(111) thin films (from Lemire, 2004 [106]). Lower panel: stable step geometries for these surfaces.

monoatomic step. The lower part of Figure 15.23a shows an atomically resolved STM image of an MgO(100) surface exposing a regular step edge. Only one type of surface ion is imaged here (Sterrer, M. and Freund, H.-J., unpublished). As the step ions are coordinatively more unsaturated than those on the regular terrace, structural relaxation around the step is to be expected. Some theoretical studies [101–103] have addressed this point and the results are depicted in the inset in Figure 15.23a, showing in gray the atomic positions of the unrelaxed step and in black those after relaxation. The ion displacement amounts to only a small percentage of the interionic distance; however, as can be inferred from Figure 15.23, it goes in directions that tend to smooth out the step and make it more round.

For rutile, as a more complex oxide crystal structure, STM of TiO₂(110) (Figure 15.23b) reveals also the occurrence of monoatomic steps only; however, in this case, several different step directions and step terminations are possible [104]. The most common steps observed run along [001] and [1–11]. The atomic step configurations shown in Figure 15.23b have been constructed applying the concept of autocompensation, that is, breaking the same amount of Ti → O and O → Ti bonds. This criterion is fulfilled for steps along [1–11] and for [001] if it is cut next to the Ti atoms underneath the bridging oxygen. The second possibility to obtain steps in [001] direction is a cut between the in-plane oxygen and titanium atoms. This step is not autocompensated and consequently tends to reconstruct, yielding a step edge shown in the inset of the STM image and the atomic configuration in Figure 15.23b.

Determination of step geometries becomes more difficult with increasing complexity of the oxide crystal structure. Henrich and Shaikhidinov [105] have estimated the stability of possible step configurations on Fe₃O₄(111), which exhibits the inverse spinel structure, by considering the excess charge and coordinative unsaturation of different step geometries. In Figure 15.23c, an STM image and a model of the Fe₃O₄(111) surface is shown [106]. Normal to the (111) surface, the crystal structure consists of close-packed oxygen planes, which are separated by two alternating types of iron planes, one containing only octahedrally coordinated Fe and the other consisting of one plane of octahedral Fe and two planes of tetrahedral Fe. From STM studies, it was concluded that the steps run along <–110> type directions. The step height between two adjacent terraces was determined to be ~4.8 Å, which corresponds to the repeat unit of the bulk crystal structure. For the analysis of step stability, 10 different step geometries have been considered and analyzed with respect to their excess charge and coordinative unsaturation. The steps shown in the lower part of Figure 15.23c are considered to be the most stable step structures on Fe₃O₄(111) based on this analysis.

Point Defects – Oxygen Vacancies Two fundamentally different situations occur for oxygen vacancies on the oxides of transition metals and non-transition metals. Formally, the removal of an oxygen atom leaves behind two electrons on the surface. On the surface of MgO, for example, one or two electrons may remain trapped in the vacancy, a consequence of the high degree of ionicity and the high Madelung

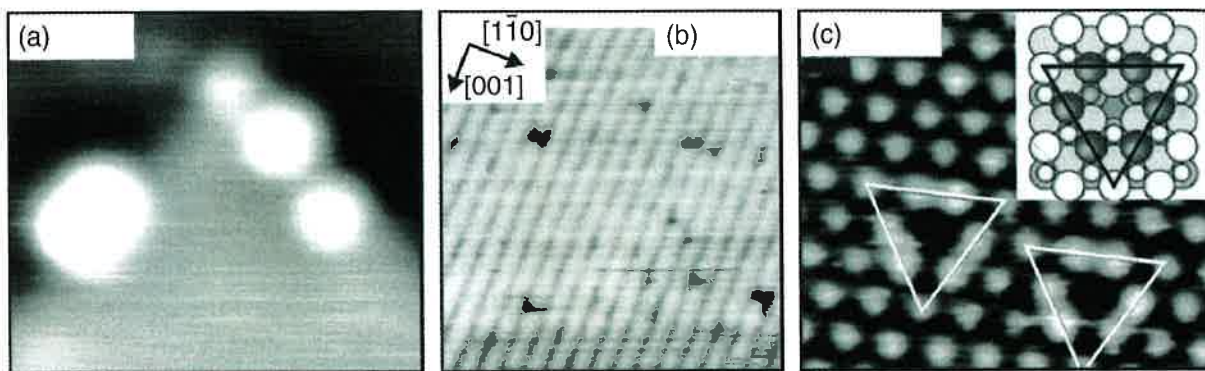


Figure 15.24 Scanning probe microscopic images of point defects on oxide surfaces: (a) MgO(001) thin films ($5 \times 5 \text{ nm}^2$) (from Sterrer, 2006 [107]), (b) $\text{TiO}_2(110)$ ($10 \times 10 \text{ nm}^2$) (from Fukui, 1997 [109]), and (c) $\text{CeO}_2(111)$ ($4 \times 3.5 \text{ nm}^2$) (from Esch, 2005 [115]).

potential (stabilization of the charged entity by electrostatic interaction with the surrounding ions). On the other hand, reducible transition metal ions such as in TiO_2 or rare earth metal ions such as in CeO_2 are capable of trapping the electrons, thus changing their oxidation state. In this case, the charge is not confined at the vacancy position but distributed among the next-nearest neighbor metal ions. Oxygen vacancies, therefore, lead to new states in the electronic structure of the oxide surfaces, either localized trap states or reduced metal oxidation states, which, if abundant in high enough quantities, are accessible to spectroscopic detection. The electronic properties of point defects will be discussed separately later.

Recently, attempts to resolve point defect structures on oxide surfaces by microscopic techniques (AFM and STM) have been undertaken. Figure 15.24 shows a collection of scanning probe microscopic images of surface oxygen vacancies on different oxides. On the surface of MgO thin films, protrusions that can be seen at specific bias conditions in STM have been attributed to electrons trapped in oxygen vacancies or related features. The STM image in Figure 15.24a shows that these protrusions are located at the step and corner sites of MgO islands [107], which is consistent with the higher stability of oxygen vacancies at these surface sites [103, 108], but similar defects have also been observed on terrace sites. However, in the case of MgO(100), attempts to resolve oxygen vacancies with atomic resolution have not been successful up to now.

Figure 15.24b shows an AFM image of the $\text{TiO}_2(110)$ surface. The bright lines running across the image are identified as rows of bridging oxygen characteristic of the (110) rutile surface (Figure 15.5) [109]. The dark contrast appearing on the bridging oxygen rows was assigned to missing oxygen. This interpretation was recently confirmed by AFM simulations that show that the interaction forces between tip and surface are largest above the bridging oxygen sites [110]. It should be mentioned here that a similar structure, but with reversed contrast (bridging O rows appear dark), is observed with STM applying positive bias voltage, because in this case tunneling occurs via the empty Ti states [111]. Oxygen vacancies have also been identified by STM on $\text{TiO}_2(110)$; however, they react instantaneously

with residual water molecules even under good UHV conditions to form surface hydroxyl groups with similar image contrast. For a discussion concerning STM imaging of missing oxygens and hydroxyl groups on $\text{TiO}_2(110)$, see Ref. [112] and references therein.

On the surface of $\text{CeO}_2(111)$, which is a relatively open surface with a large corrugation, single and multiple vacancy defects both on the surface and in the subsurface layer have been atomically resolved by STM and AFM [113–115]. Figure 15.24c shows an STM image of the $\text{CeO}_2(111)$ surface with two single oxygen vacancies recorded at bias conditions where oxygen ions are imaged [115], therefore showing dark contrast at the position of the vacancy within the hexagonal arrangement of surface oxygen ions.

The geometric relaxation around oxygen vacancies on oxide surfaces follows the trend seen above for steps, that is, the neighbor ions are slightly displaced such that the vacancy geometry becomes more round. In general, the next-neighbor metal ions move slightly outward and the oxygen ions in the second coordination sphere are displaced inward. This behavior is found from calculations of the structural relaxation of oxygen vacancies on the MgO surface. Depending on the charge state of the vacancy, the magnitude of the displacement differs, being small for the neutral oxygen vacancy that contains two trapped electrons and larger for the positively charged vacancies that contain only one or no electron [116]. A similar behavior in terms of displacements of cations and anions around the defect is found for the oxygen vacancy on $\text{CeO}_2(111)$, with the difference that here electrons are trapped on two of the three next-nearest cerium ions, which reduces the formal ionic charge of those from +4 to +3. This breaks the local hexagonal symmetry around the defects, as the ionic radius of the Ce^{3+} ions is larger than that of Ce^{4+} , leading to different bond lengths [117, 118]. Several theoretical studies have also aimed at determining the relaxation around a missing oxygen on $\text{TiO}_2(110)$ [119–122]. There is general agreement that the cations underneath the missing oxygen relax away from the defect, in line with the considerations for the oxygen vacancies on MgO(100) and $\text{CeO}_2(111)$. Most of the theoretical studies have considered an array of vacancies with high vacancy concentration. The relaxation of oxygen ions in these cases depends on the interaction between vacancies and, therefore, does not reflect the situation of an isolated vacancy. In the study, where an isolated vacancy was considered, only the relaxation of the Ti ion underneath the oxygen vacancy was published.

15.3

Electronic Structure of Oxide Surfaces

As stated in the introduction, oxides may cover a wide range of electronic properties, in particular, from insulating ionic to superconducting materials. Consequently, the electronic structure of oxides covers wide band gap insulators, semiconductors, and metals. Examples are MgO or Al_2O_3 , which show properties of insulators with band gaps of 7.5 and 8.5 eV [123], respectively; TiO_2 or TiO_3 with semiconducting

properties due to their bandwidth of around 3 eV; and RuO_2 representing a metallic oxide. In addition, the electronic properties may be tuned by doping the bulk with appropriate dopants, so as to change conductivity and also optical properties. For a discussion of the bulk electronic properties of oxides and the different models to describe the electronic structure, we refer the reader to Refs. [1, 2, 9].

Through the formation of surfaces, bonds are broken and the above-addressed relaxations, rumpling, or reconstruction phenomena affect the interatomic potentials and bonding characteristics. The surface electronic structure is modified with respect to the bulk. In the following, we will address a few topics connected with surface electronic structure of some selected oxides.

15.3.1

Valence Electronic Structure

As an example to study the valence electronic structure of oxides, we consider one of the least disturbed and relaxed surfaces, namely, the $\text{MgO}(100)$ surface. Figure 15.25a shows angle-resolved photoemission (Volume 1, Chapter 3.2.2) data taken with HeII radiation at different polar angles θ along the $\Gamma \rightarrow X$ azimuth defined in the figure [124]. Via the simple formula

$$k_{\parallel} = \left(\frac{2m}{\hbar^2} E_{\text{kin}} \right)^{1/2} \sin \theta \quad (15.3)$$

the observed peak positions can be transferred into an E versus k_{\parallel} band structure diagram. The observed dispersions are superimposed onto a projected band structure (Figure 15.25b). The projection is from bulk MgO onto the (100) surface. In the diagram, the states resulting from the existence of the surface (small squares)

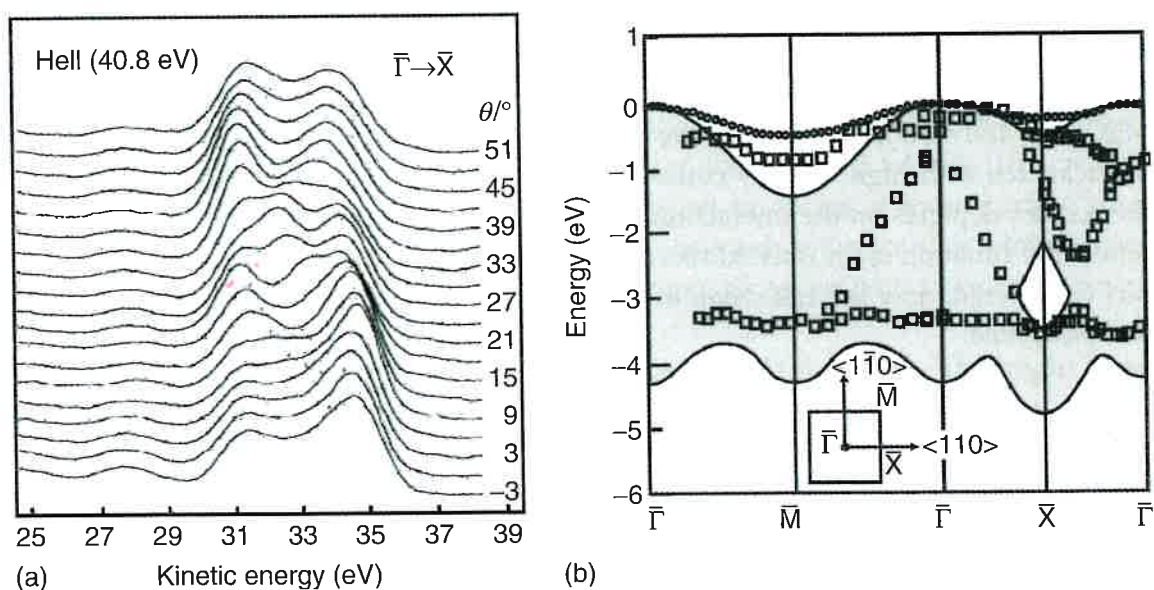


Figure 15.25 (a) Angular resolved UPS spectra of the $\text{MgO}(100)$ surface [124]. (b) Projection of the ARUPS (angle-resolved ultraviolet photoelectron spectroscopic) data (large squares) and calculated surface state dispersion (small squares) on the bulk electronic structure of MgO ; from Tjeng, 1990 [124], Schönberger, 1995 [125].

are shown [125]. Obviously, in the experiment, one observes features resulting from bulk states *and* from surface states. The surface phenomena are enhanced because the kinetic energy of the electrons is near the minimum of the universal curve for their mean free path. In certain areas of the surface Brillouin zone (SBZ), the surface states are situated slightly above the valence band edge, within the gap of the material. The reason for the shift of the surface state away from the bulk states is clear: as MgO is a largely ionic material with rock salt structure, the creation of a (100) surface eliminates, in the ideal case, one nearest neighbor for each surface ion, that is, both oxygen and magnesium. This reduces the Madelung potential felt at the respective ion positions and leads to a smaller binding energy of the states resulting from the interaction of those ions. Note that this is only true for the ideal (100) surface. On a real surface, one will encounter steps, edges, and kinks, where the coordination of the respective ions are different. Localized states due to such defects will naturally also be situated within the gap and spread the energy of states characteristic of the surface.

As a second example, we consider a semiconducting oxide, namely, ZnO. Here, we discuss the electronic band structure as again revealed by photoemission and shown in Figure 15.26 [126]. The features between 3 and 9 eV binding energy originate from states formed within the oxygen sublattice, of course, hybridized with Zn 4s electrons. The Zn 3d states lead to a sharper feature below 10 eV binding energy. The spectra are taken on a ZnO single crystal exposing the (10–10) surface, which is the most stable low-index surface of ZnO in the wurtzite phase. The structure is schematically shown in the insets in Figure 15.26. The surface is characterized by alternating rows of coordinatively unsaturated O and Zn atoms with occupied and unoccupied dangling bond orbitals aligned along the [1–210] direction. These dangling bond orbitals are characteristic of the surface and are the basis for the existence of extended surface states. Feature A in Figure 15.26 has

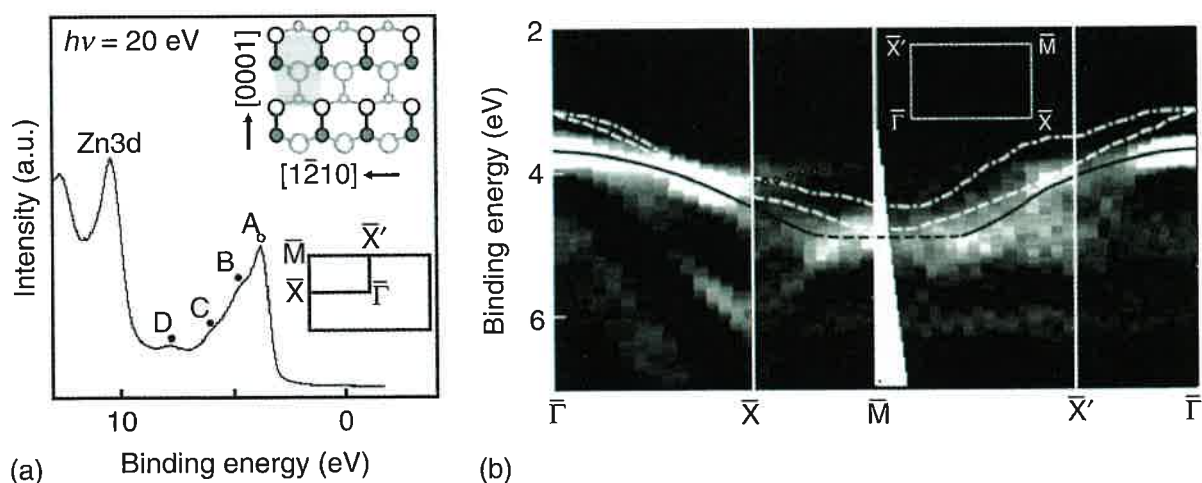


Figure 15.26 (a) Normal emission UPS spectrum of ZnO(10–10). (b) Intensity plot of ARUPS spectra from ZnO(10–10) along the high symmetry directions. The white lines indicate the upper edge of the projected bulk valence band. The black line indicates the dispersion of the surface state observed on ZnO(10–10); from Ozawa, 2005 [126].

been identified to be a two-dimensional surface state: the feature does not show any dependence in its energetic position on changing the photon energy to excite the photoemission spectrum in normal emission. This indicates the two-dimensional nature of the state, that is, no coupling to bulk states at Γ . In addition, the intensity of the feature is sensitively attenuated on adsorption of species from the gas phase. Features B, C, and D are associated with bulk band emissions. Figure 15.26b shows the observed E versus k_{\parallel} dispersion of the surface state along high symmetry directions of the SBZ. Its dispersion is indicated by the black line and can be understood based on the overlap anisotropy of neighboring dangling bond orbitals in the $[1-210]$ and $[0001]$ directions. The white lines mark the projected bulk valence band edge of ZnO as obtained from calculations [83, 85], showing that the surface state is located below the valence band edge, in contrast to the MgO example discussed earlier.

Photoemission provides detailed insight into the electronic structure of surfaces. The two case studies discussed above for an insulating and a semiconducting oxide exemplify this. For metals and adsorbates thereupon, this had been demonstrated for many cases (Volume 2, Chapter 5). We, therefore, refrain from showing yet another example for a metallic oxide.

15.3.2

Surface Excitation

Photoemission, however, is not the only tool to study surface electronic structures. Inelastic electron scattering may also be used to study surface-induced phenomena including surface excitons and charge-transfer excitations. Figure 15.27 shows two examples for such phenomena. In Figure 15.27a, an electron energy loss spectrum obtained on MgO(100) is shown [127]. The sharp rise in scattering intensity at a loss

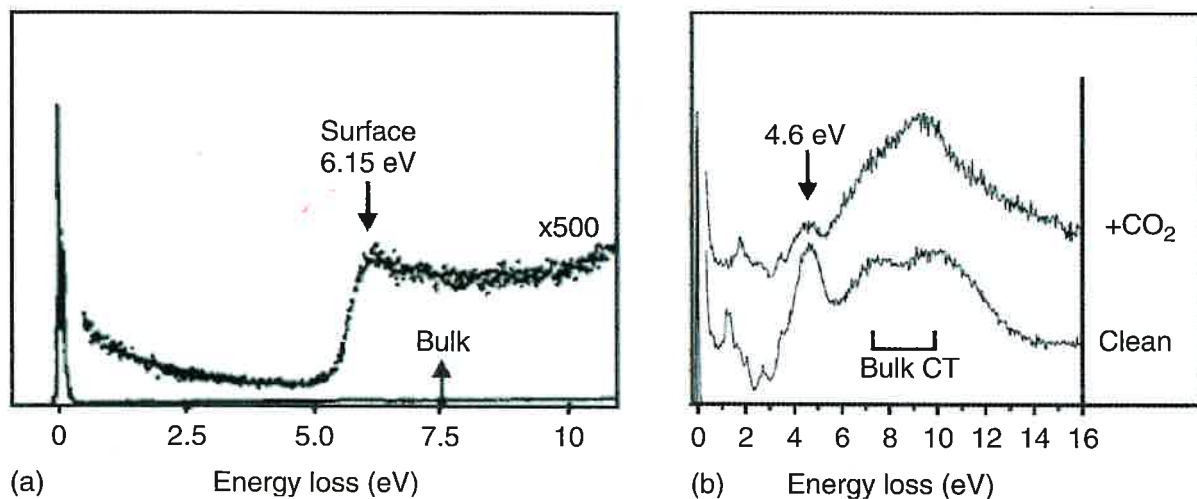


Figure 15.27 (a) Electron energy loss spectrum from the MgO(100) surface showing a loss peak at 6.15 eV, which is considerably lower in energy than the bulk band gap; from Cox, 1986 [127]. (b) Electron energy loss spectra of a clean and CO₂-covered Cr₂O₃(0001) surface; from Mejias, 1999 [131].

of 6.15 eV marks the onset of the band gap. As indicated, this value is considerably different from the one observed via optical spectroscopy in the bulk. The reason is due to a phenomenon already briefly mentioned earlier: at the surface, the O and Mg ions feel a different Madelung potential as compared to the bulk, which destabilizes the surface with respect to the bulk. If under such conditions electrons are excited across the band gap, the electron–hole pairs created are at lower energies as compared with bulk band gap excitations. The localization in the surface leads to the so-called surface excitations whose energies depend on the particular coordination of the ions at the sites where they are created [128]. Therefore, excitations at regular surface sites have an energy different from those at steps, kinks, or edges, which in turn leads to a spread of excitations over a range of energies below the bulk band gap excitation. In fact, by designing surfaces with an engineered defect density, one will be able to differentiate these different contributions to the intensity below the band gap excitation. Using nanocrystalline material, this has already been possible to a certain extent [129]. It is possible with an STM tip to locally excite specific sites in the surface and observe the fluorescence from the excitation by recording spatially resolved and energy-resolved photon maps. If this can be done with sufficiently high spatial resolution, a detailed assignment of excitation energies to particular sites will be possible [130].

Figure 15.27b shows another example of an electron energy loss spectrum of a wide band gap insulator, namely, $\text{Cr}_2\text{O}_3(0001)$ [131]. Again the material has been grown as a thin film. Here, a complication, as compared with the previous example, comes into play. $\text{Cr}_2\text{O}_3(0001)$ contains partially filled d-shells, which give rise to weak d–d excitations in the band gap. This particular aspect will be discussed in depth in the following section in connection with $\text{NiO}(100)$. Here, we would like to focus on another aspect connected with charge-transfer excitations from the localized d-states at the Cr cations to the oxygen atoms in the surface. Again, the Madelung potential at the surface is different from that in the bulk. In addition, the symmetry at the surface is different from that in the bulk, which allows for additional dipole transitions. It is the lowering of the Madelung potential that lowers the excitation energies with respect to the bulk when an electron is transferred from the fully occupied oxygen orbitals to the partially filled Cr cations. On the basis of theoretical studies, the observed states in the bulk band gap of $\text{Cr}_2\text{O}_3(0001)$ have been assigned in detail by Staemmler and coworkers [16].

15.3.3

Localized d–d Excitations in Transition Metal Ions

We have discussed electronic transitions in insulators resulting from oxygen valence band electrons either in the form of charge transfer into unoccupied metal states or as localized excitons. These transitions more or less scale with the width of the band gap. In transition metal oxides, on the other hand, localized intra-atomic transitions within the d manifold of electronic states are possible

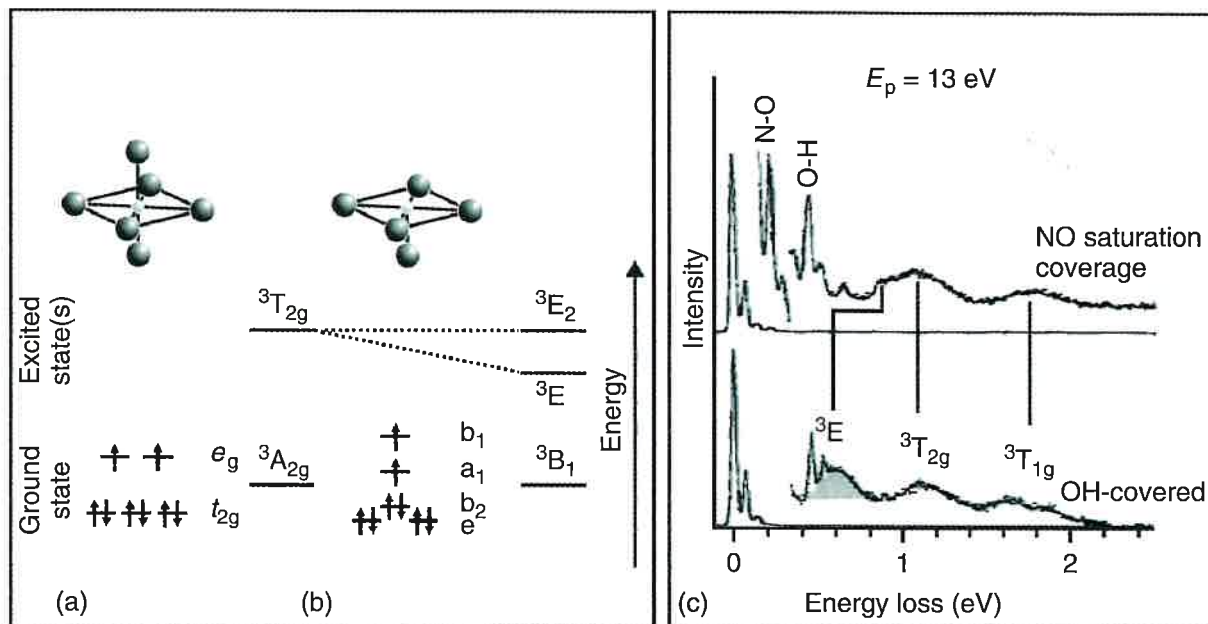


Figure 15.28 Comparison of orbital diagrams and energies of the ground state and electronically excited states for (a) NiO bulk and (b) NiO(100). (c) Electron energy loss spectra taken on adsorbate-covered NiO(100) thin films: lower trace, OH-covered before NO adsorption; upper trace, after NO saturation coverage; from Freitag, 1993 [132].

due to only partially filled d-bands in these materials. Consider first the situation encountered in the bulk for NiO as an example. Here, the Ni ion is embedded in the symmetric octahedral environment of six next-nearest oxygen ions or ligands. This leads to a splitting of the five d-orbitals into two sets, denoted as t_{2g} and e_g (ligand field splitting or crystal field splitting). The d^8 ground-state configuration of Ni^{2+} is a $^3A_{2g}$ state with a completely filled t_{2g} subset and two unpaired electrons in the e_g -orbitals. The first excited state, $^3T_{2g}$, corresponds to a state where one electron is transferred from the lower t_{2g} into the upper e_g level (Figure 15.28a). The surface Ni ion, on the other hand, has lost one of its next-nearest oxygen neighbors, with a concomitant reduction of the symmetry. This affects also the energy of the d electronic levels. In an orbital picture, this can be rationalized by the different symmetries of the 5d orbitals and their orientation with respect to the oxygen ligands in an octahedral environment. Owing to the reduced symmetry on the surface, the t_{2g} and e_g subsets split further into e and b_2 , and a_1 and b_1 levels, respectively (Figure 15.28b) [132]. The energy for exciting an electron from the highest filled level to the lower single-occupied level is, therefore, substantially less than the lowest transition for a bulk Ni ion.

Experimentally, this behavior has been observed for d–d excitations measured with electron energy loss spectroscopy (EELS), for example, for NiO(100) [132, 133], CoO(100) [134], and $Cr_2O_3(0001)$ [135]. In Figure 15.28c, experimental results obtained on localized d–d transitions for the surface of NiO(100) thin films grown on Ni(100) are shown. The region below 0.5 eV is characterized by phonon losses

in the NiO bulk and by adsorbate vibrations. The lower part of Figure 15.28c shows the spectrum of a NiO(100) surface that has been covered by OH groups in order to saturate defects on the surface. The energy loss spectrum of this surface above 0.5 eV shows three distinct loss peaks at 0.6, 1.1, and 1.8 eV. Using spin-polarized EELS, the last two transitions could be assigned to the $^3T_{2g}$ and $^3T_{1g}$ bulk excitations [136, 137], which is confirmed by adsorption experiments using NO (Figure 15.28c) that show that these two transitions remain unchanged on adsorption. On the other hand, the transition at 0.6 eV is sensitive to adsorption of NO. The excitation energy is shifted from 0.6 eV in the lower spectrum in Figure 15.28c to 0.9 eV on the NO-covered surface. This proves, therefore, that this transition is related to a surface-specific contribution. The experimental results have been confirmed by cluster calculations, which could identify the low-energy surface transition according to the aforementioned considerations (Figure 15.28b). Additionally, the shift of the surface excitation to energies close to the first bulk transition on adsorption of NO has been shown to result from the restoration of the bulk coordination environment of the surface Ni^{2+} ion by the attachment of the NO molecule.

15.3.4

Core-Level Shifts

We have seen earlier that under certain conditions, the corundum-type surfaces have stable surface geometries that do not correspond to a bulk-terminated plane but contain oxygen double-bonded to the surface metal ions, $Me=O$ (e.g., chromyl-, ferryl-, and vanadyl-terminated $Me_2O_3(0001)$ surfaces). The coordination of the surface metal ions is increased from 3 to 4 by bonding to additional oxygen. Moreover, its oxidation state is changed from formally +3 to +5. The change in the oxidation state can be observed by shifts in the core-level binding energies with XPS. In Figure 15.29, this is exemplified for $V_2O_3(0001)$, by comparison of the V2p XP spectra of the vanadium- and vanadyl-terminated surfaces of $V_2O_3(0001)$ [75]. The spectra have been collected both at normal emission, $\theta = 0^\circ$, which is sensitive to bulk and surface, and at grazing incidence, $\theta = 70^\circ$, for enhanced surface sensitivity. At normal emission, the vanadyl-terminated surface shows a V2p_{3/2} emission peak with a chemical shift that is typical for V^{3+} . If we compare this spectrum with the one obtained from the same surface under surface-sensitive conditions (Figure 15.29b), we see that in the latter, a pronounced shoulder on the high-energy side appears, which is not observed for the metal-terminated $V_2O_3(0001)$ surface under similar emission conditions (Figure 15.29c). The attenuation of the high-energy shoulder when going from surface sensitive to normal emission directly reflects the surface nature of this component and, thus, can be attributed to the presence of the vanadyl groups. The binding energy of the vanadyl-induced peak as obtained from the spectral fits (Figure 15.29b) is comparable to the V2p_{3/2} binding energy of V^{5+} in V_2O_5 (Figure 15.29d), giving evidence for the changed oxidation state of vanadium ions on the vanadyl-terminated surface.

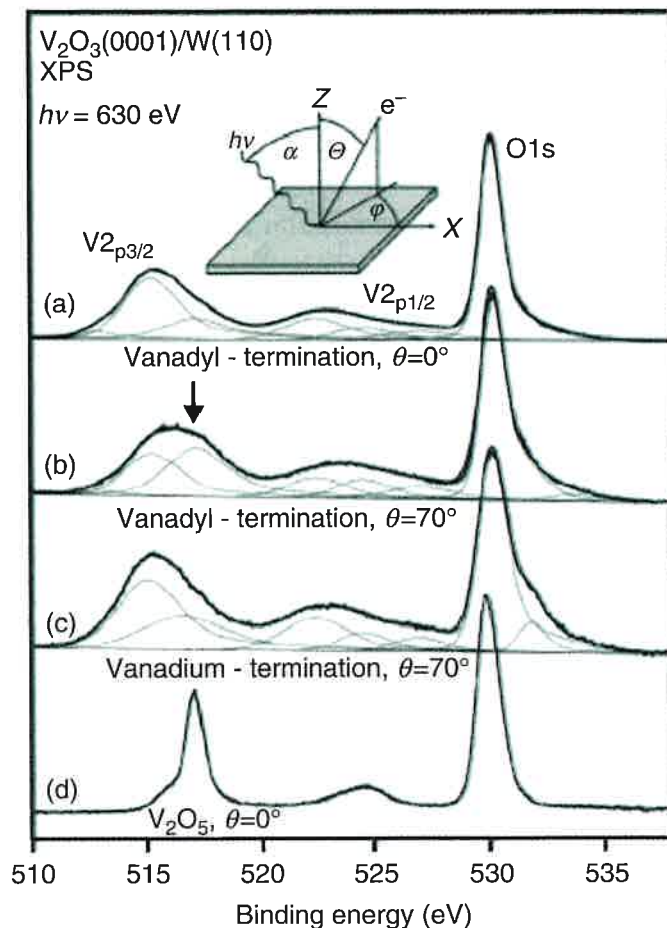


Figure 15.29 XPS spectra of the vanadyl- (a,b) and vanadium-terminated $V_2O_3(0001)$ surface (c) showing a characteristic shift of $V2p_{3/2}$ emission of the vanadyl-terminated surface to higher binding energies, which indicates a change in the oxidation state. As a reference in (d), the XPS spectrum of V_2O_5 is shown; from Guimond, 2006 [75].

15.3.5

Effect of Surface Structure on Bulk Electronic Properties

Several transition metal oxides undergo a metal-to-insulator transition (MIT) depending on temperature or pressure. One of the most widely studied oxides in this respect is V_2O_3 , which shows a transition from a paramagnetic metallic to an antiferromagnetic insulating state at $T = 150$ K. In several studies, using UPS, this transition has been proved experimentally by mapping the density of states near the Fermi level, and in a theoretical study, combining the local density approximation with dynamical mean field theory [138], the experimental results could be well reproduced. An MIT is, of course, a bulk property; however, electron density near the Fermi level is preferably measured with UPS, which is also a surface-sensitive method. One might ask, therefore, the question how the structure of the surface influences the bulk electronic properties. The effect of surface reconstruction has been shown by STS and UPS for two differently prepared (0001) surfaces of V_2O_3 to have a considerable effect on the electronic density of states at the Fermi level, where for one surface a gap state and for the

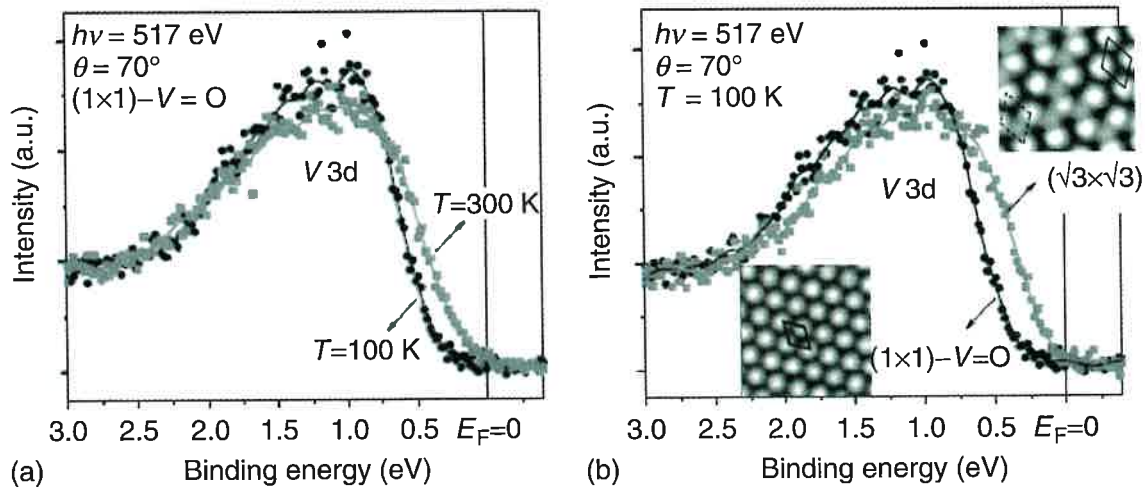


Figure 15.30 (a) Valence band photoemission spectra of the vanadyl-terminated $V_2O_3(0001)$ surface below (100 K) and above (300 K) the metal-to-insulator transition temperature. (b) Comparison of the VB spectra from a vanadyl-terminated and $(\sqrt{3} \times \sqrt{3})$ -reconstructed $V_2O_3(0001)$ surface taken at 100 K; from Pfuner, 2005 [140].

other a metallic behavior at room temperature was observed [139]. This study, however, lacks from a detailed characterization of the surfaces used. More recently, the effect of the surface structure on the MIT was studied for two atomically characterized terminations of $V_2O_3(0001)$ both above and below the transition temperature, the results of which are shown in Figure 15.30 [140]. The two surfaces that have been studied are the (1×1) vanadyl-terminated surface and a reconstructed surface that shows a regular arrangement of vanadyl groups, which is also termed the $(\sqrt{3} \times \sqrt{3})$ oxygen-rich $V_2O_3(0001)$ surface (see insets in Figure 15.30b). Figure 15.30a shows the differences in the density of states measured by UPS under surface-sensitive conditions for the metallic (300 K) and insulating (100 K) phases of the vanadyl-terminated surface. The insulating gap that opens below 150 K is clearly discernible from the metallic behavior at 300 K, which is characterized by a finite density of states at E_F . On the other hand, the comparison of UPS spectra measured at 100 K for the vanadyl- and $(\sqrt{3} \times \sqrt{3})$ -terminated surfaces shown in Figure 15.30b gives evidence that the reconstructed surface is still metallic at this temperature.

These results show that for ideally terminated surfaces (we consider the vanadyl termination also as an ideal $V_2O_3(0001)$ termination because it represents a stable surface configuration), bulk-specific properties may also be observed on the surface. However, a perturbation of the local surface structure leads to significant changes in these properties.

15.3.6

Defects on Oxide Surfaces

We have noted when discussing the geometric structure of defects on oxide surfaces that, depending on the type of oxide, there are two different mechanisms of trapping the two electrons that remain if an oxygen atom is removed from the

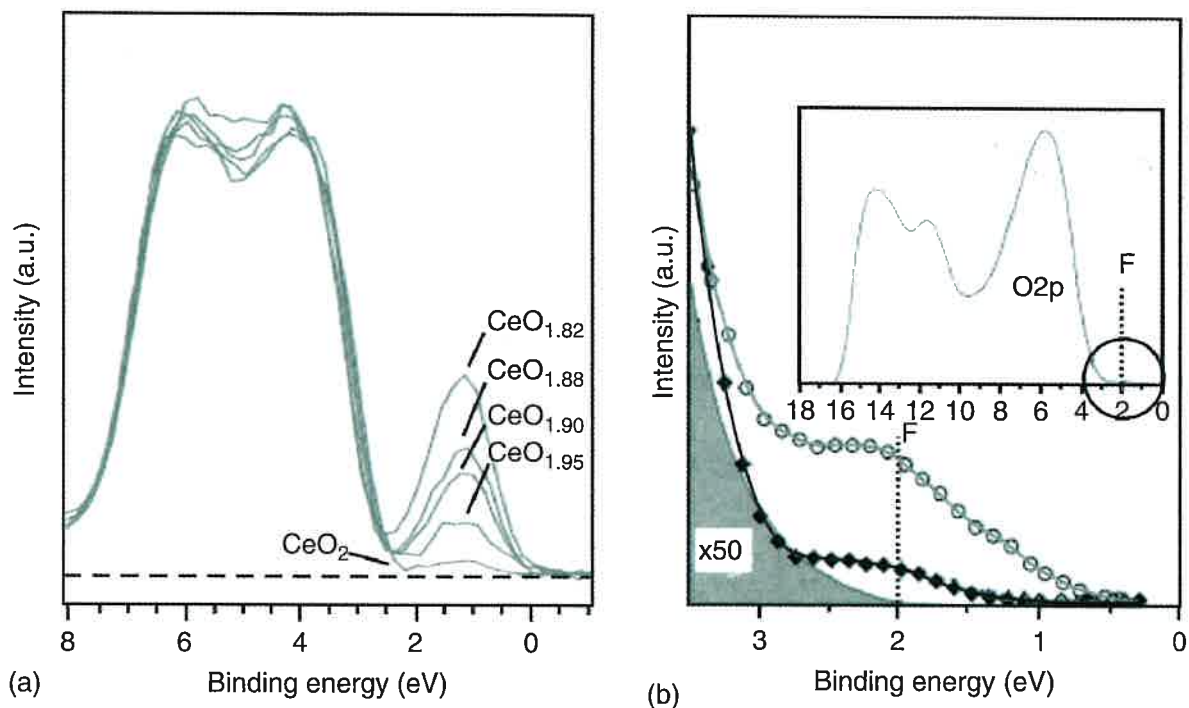


Figure 15.31 (a) Valence band photoemission spectra of the $\text{CeO}_2(111)$ surface with different surface stoichiometries; from Henderson, 2003 [139]. (b) MIES spectra of the surface of $\text{MgO}(100)$ thin films before and after electron bombardment; from Kolmakov, 2000 [142].

surface: charge trapping in the vacancy or reduction of neighboring metal ions. On transition metal oxides such as TiO_2 or CeO_2 , the electrons are trapped at metal cations leading to a change in their oxidation states, whereas on non-transition metal oxides such as MgO , electrons are trapped within the vacancy that is created by removal of an oxygen atom. Although the mechanism of charge trapping is different in these two cases, the consequences in terms of changes in the electronic structure are very similar. Both lead to localized electronic states within the band gap of the oxide. This is best exemplified by looking at the valence electronic structure as it is shown in Figure 15.31a,b for trapped electron states formed by removal of oxygen atoms on the surface of $\text{CeO}_2(111)$ [141] and $\text{MgO}(100)$ [142] thin films, respectively.

The main features in the valence band spectra of these materials result from $\text{O}2p$ states (in CeO_2 , $\text{Ce}5d$ states also contribute to the valence electronic structure), with vanishing density of states in the forbidden gap. In the case of $\text{CeO}_2(111)$ films, oxygen vacancies are generated by heat treatment between 773 and 973 K (for single-crystal samples, surface reduction is observed only after heating to 1100 K). This leads to loss of oxygen in the surface layer and a calculated surface stoichiometry as indicated in Figure 15.31a. On heat treatment, a new peak in the density of states appears above the valence band. This peak originates from the remaining electrons that occupy the lowest available energy level of Ce, which is $\text{Ce } 4f$, thus reducing Ce^{4+} to Ce^{3+} . These experimental findings could well be reproduced by calculating surface properties of $\text{CeO}_2(111)$ with DFT methods including correlation effects (the Hubbard U) [118]. In a similar way, on reduction

of the surface of $\text{TiO}_2(110)$, electrons occupy empty Ti 3d levels, leading also to a localized electronic states in the band gap resulting from Ti^{3+} . That these defects are indeed located on the surface can be shown by reoxidation using O_2 or H_2O , upon which the surface-related states completely vanish. A qualitatively similar result is obtained on the surface of $\text{MgO}(100)$ thin films, where surface reduction is achieved by electron bombardment (Figure 15.31b), leading to electron-stimulated desorption of oxygen atoms. The remaining electrons are trapped in the vacancy forming localized electronic states 1–2 eV above the valence band. The oxygen vacancy on the MgO surface is probably the most studied type of defect on oxide surfaces. In the following, a short summary of the experimental and theoretical efforts to characterize these defects is presented.

15.3.6.1 Oxygen Vacancies on the MgO Surface

On the MgO surface, oxygen vacancies can occur in three different charge states. A bare vacancy, V_a , is obtained by removal of an O^{2-} ion. Oxygen vacancies occupied by either one or two electrons are called F^+ and F^0 centers, respectively. It has been suggested for a long time that F centers exist on the surface of MgO ; however, a detailed investigation of these defects on single crystalline MgO turned out to be rather difficult. Therefore, most of the properties of F centers were extracted from theoretical studies. In Figure 15.32a, electron density plots for the three charge states of the anion vacancy on the (100) surface of MgO are shown, together with values of the electron density Q integrated within the spheres depicted in the images. From the isodensity lines, the electron localization within the vacancy is clearly evident for the F^+ and the F^0 center [116, 143, 144]. The driving force for

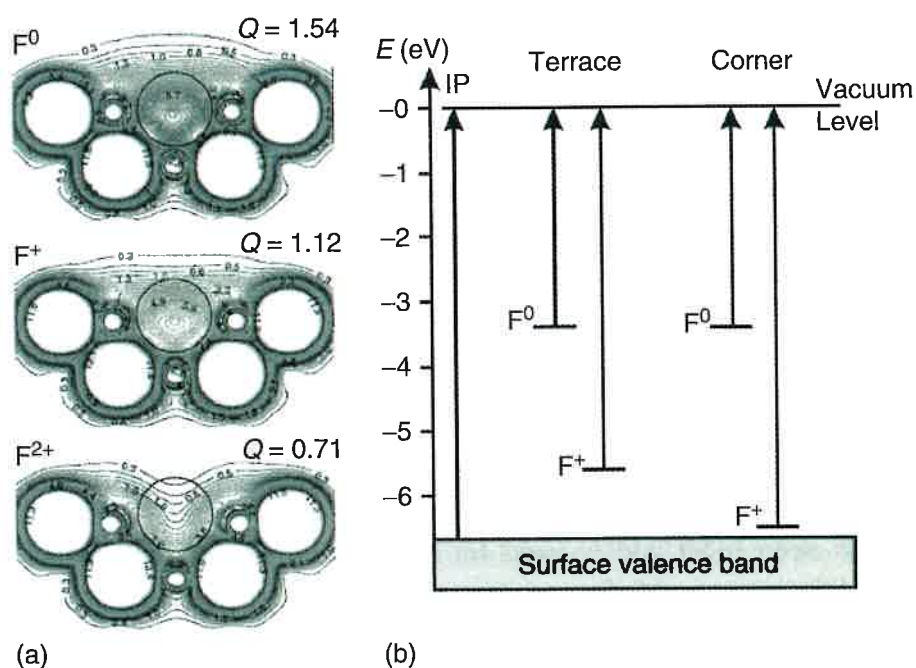


Figure 15.32 (a) Electron density plots for the three charge states of oxygen vacancies on the MgO surface. (b) Dependence of ionization potentials of electrons trapped in oxygen vacancies located in different positions on the MgO surface; from Sushko, 2000 [143].

the localization is the Madelung potential of the surrounding ions. Apart from the regular (100) surface of MgO, other locations, for example, at the edges or corners on the MgO surface, have been considered as sites for the anion vacancy defect. Figure 15.32b shows a comparison of the ionization potentials (IPs) for F^+ and F^0 centers at the (100) terrace and at an MgO corner, respectively [143]. The Madelung potential is proportional to the coordination of the respective sites, suggesting that for a three-coordinated anion vacancy at a corner, the IP should be smaller than that for the same defect on the regular (100) surface due to the reduced Madelung potential at this site. However, the calculations show that the IP at the corner is equal to (F^0) or even higher (F^+) than that for the anion vacancy on the regular terrace (Figure 15.32b), which is because at the lower coordinated site, the electron cloud extends more toward the vacuum. This leads to smaller exchange and Coulomb's repulsion with the neighboring ions and, therefore, a higher stability. It has been found that almost all properties related to electrons trapped in anion vacancies depend more or less on the coordination of the defect site. For example, the formation energy of anion vacancies decreases in the series as terrace (where the oxygen ion is fivefold coordinated, 5C) \rightarrow edge (4C) \rightarrow corner (3C), implying that defects located at lower coordinated sites are more stable than those at higher coordinated ones. Correspondingly, vacancies tend to diffuse from the bulk to the surface, and there from the higher to the lower coordinated sites [103, 108, 143–145]. The same dependence on coordination number is also found for the optical excitation energy of F^+ and F^0 centers, which is highest for the terrace defect and lowest for the corner defect [146, 147].

For the experimentalist, F^+ and F^0 centers are most interesting because they represent spectroscopically active species. Both exhibit electronic transitions in the visible range of the optical spectrum, and the F^+ center is, due to its unpaired electron, a paramagnetic entity that can be investigated by electron paramagnetic resonance (EPR). Optical absorption and EPR have been extensively used to characterize F centers in the bulk of MgO single crystals. With the advent of MgO thin films, this insulating oxide became also accessible to classic surface science spectroscopic tools that made experimental characterization of surface F centers possible.

Until now, there is no experimental evidence for a rich abundance of F centers (at least within the experimental detection limit) on freshly prepared MgO thin films. Methods that have been described in the literature to produce F centers on MgO thin films include high-temperature annealing and subsequent quenching, electron bombardment, or Ar^+ bombardment. Among these methods, electron bombardment has been most widely used for the generation and subsequent characterization of F centers on MgO.

With metastable impact electron spectroscopy (MIES) and UPS, an additional electronic state within the band gap, about 1–2 eV above the O2p valence band, of MgO thin films has been detected and attributed to F centers (Figure 15.31b) [142]. The position of the defect-related peak within the MgO band gap is in line with theoretically predicted energy levels of F centers in MgO. However, the signals are

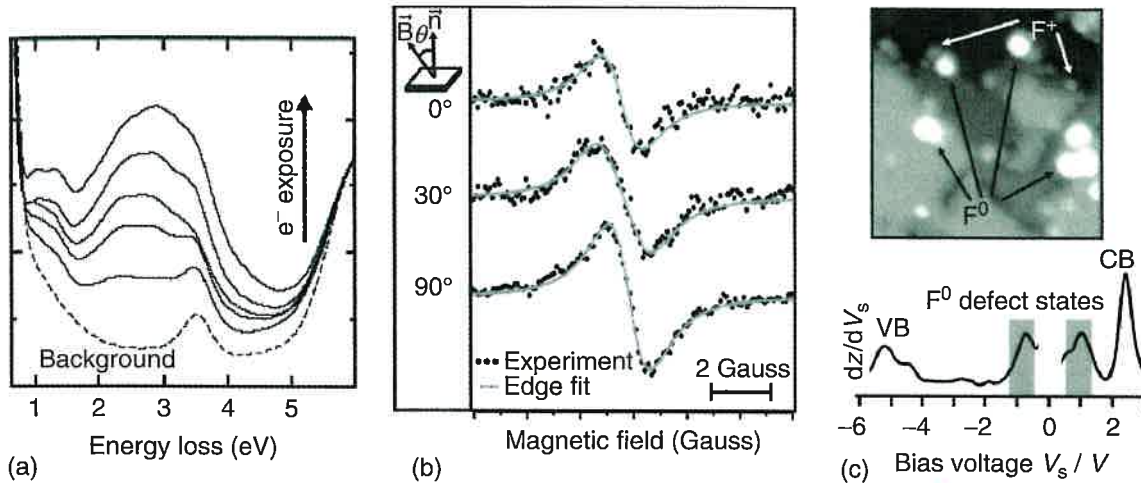


Figure 15.33 (a) Electron energy loss spectra of MgO(001) thin films subjected to electron bombardment; from Kramer, 2002 [148]. (b) Electron spin resonance spectra of F^+ centers on the surface of MgO(001) thin films; from Sterrer, 2005 [150]. (c) STM image of MgO(001) thin films with F centers and tunneling spectrum of an F^0 center; from Sterrer, 2006 [107].

very broad, and therefore, no further characterization in terms of the location of the defects is possible. Electronic excitations of color centers have been studied by EELS. Figure 15.33a shows the resulting EEL spectra obtained after electron bombardment of MgO films grown on Ag(100) [148]. With increasing electron exposure, broad loss features ranging from 1 to 4 eV appear in the spectrum, resembling the heterogeneity in transition energies and, consequently, in defect geometries. In comparison with calculated electronic transitions of F centers on the MgO surface, the loss features were assigned to excitation of F centers located on the regular (100) terraces, as well as on step edges and corners. In a subsequent study on MgO films grown on a vicinal Ag(1,1,19) substrate, where the step density of MgO is increased substantially, the assignment of the loss features to differently coordinated F centers was further approved [149].

Only recently, a detailed characterization of F centers with respect to their location and charge state on MgO thin films became possible using EPR and low-temperature STM. Figure 15.33b shows a set of EPR spectra at different angles between the static magnetic field and the surface obtained from a 20 ML thin MgO film that has been subjected to electron bombardment with 100 eV energy [150]. The signal results from F^+ centers originating from single electrons trapped on the surface. Owing to the single-crystal nature of the samples used in this experiment, the location of the defect centers could unambiguously be determined from the angular dependence of the shape and line width of the EPR signals. From a comparison of the experimental spectra with spectral fits, it was concluded that most of the defects are located at the steps of MgO islands with a small contribution of maximum 20% of the defects located on step corners. These findings were corroborated by low-temperature STM investigations on MgO thin films [107]. Figure 15.33c shows an STM image of a 4 ML thick MgO taken at a bias voltage of -3 V. At these tunneling conditions, both F^+ and F^0 centers become visible

in STM, the former giving rise to small dim spots, whereas the latter appear as large protrusions. Characterization of single defects in terms of their electronic properties is possible by performing local tunneling spectroscopy. A corresponding spectrum of an F^0 defect is shown in Figure 15.33c, where two defect states within the band gap of MgO are detected. The one below the Fermi level E_F corresponds to the occupied level, whereas the one above E_F originates from the empty defect states.

15.4 Phonons at Oxide Surfaces

Structure and lattice dynamics are intimately related, and it is therefore near at hand to investigate oxide surface vibrations. This necessitates to familiarize ourselves with the concept of surface phonons (Volume 2, Chapter 8.2). For the basics, we refer to the textbook literature. Phonons, that is, the vibrational “normal modes” of a translational invariant material, are usually discussed in terms of E versus k_n diagrams, very similar to the approach to electronic structure [151–153]. Figure 15.34 shows calculated phonon dispersion curves for an MgO(100) surface. The bulk vibrations give rise to broad bands indicated by the gray lines [154–156]. The surface vibration dispersions are given by black lines. For a calculation to show agreement to the experiment, it is of course important to perform the calculation based on the correct surface structure, that is, for MgO, a slightly ruffled surface. Most of the surface modes are located within the regime of the projected bulk vibrations. At the bottom of the bulk acoustic branch, a surface vibration is split off from the bulk phonon dispersions, which is thus easily accessible to measurements. This is the so-called (acoustic) Rayleigh mode. It involves close to $K=0$, for example, at $\omega = 2.56$ THz, acoustic phonon modes with vibrations of Mg and O atoms of similar amplitudes [154]. The amplitude decreases on

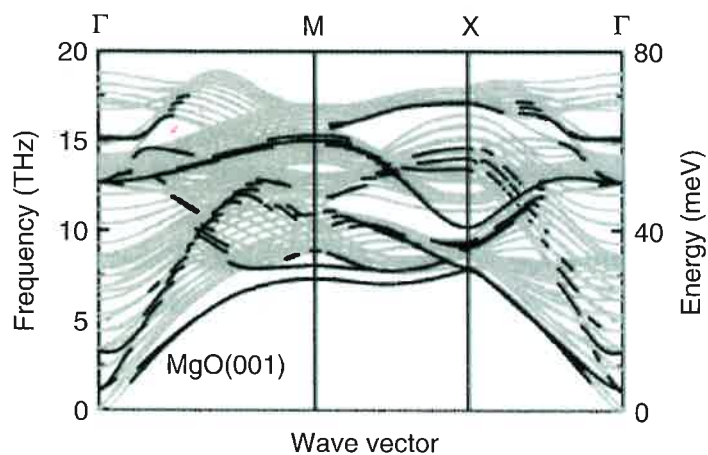


Figure 15.34 Phonon dispersion relations of the MgO(001) model for a thick (208 atoms) slab consisting of 30 and 78 curves. Solid lines correspond to surface modes; from Parlinski, 2006 [154].